AGU ADVANCING EARTH AND SPACE SCIENCES

Earth's Future

RESEARCH ARTICLE
10.1029/2025EF007809

Elevation-Dependent Permafrost Thaw on the Tibetan Plateau Delays Seasonal Discharge and Poses a Risk of Reduction in Downstream Water Availability

Chengwei Wan[1,2,3], John J. Gibson[4], Peng Yi[1], Xicai Pan[3], Chenghao Chen[5], and Grzegorz Skrzypek[2]

[1]National Key Laboratory of Water Disaster Prevention, Hohai University, Nanjing, China, [2]West Australian Biogeochemistry Centre, School of Biological Sciences, The University of Western Australia, Perth, WA, Australia, [3]State Key Laboratory of Soil and Sustainable Agriculture, Institute of Soil Science, Chinese Academy of Sciences, Nanjing, China, [4]InnoTech Alberta, Victoria, BC, Canada, [5]Department of Geotechnical Engineering, Nanjing Hydraulic Research Institute, Nanjing, China

Key Points:

- Multi-decadal runoff records, lake inventory dynamics, and isotopic tracers reveal catchment-scale hydrological changes
- Space-for-time approach with machine learning tracks permafrost thaw impacts and water yield changes across the landscape
- Advanced thaw reduces lowland runoff, causing delayed seasonal flow and decrease in basin-scale water yield

Supporting Information:

Supporting Information may be found in the online version of this article.

Correspondence to:

G. Skrzypek and P. Yi,
grzegorz.skrzypek@uwa.edu.au;
pengyi1915@163.com

Citation:

Wan, C., Gibson, J. J., Yi, P., Pan, X., Chen, C., & Skrzypek, G. (2026). Elevation-dependent permafrost thaw on the Tibetan Plateau delays seasonal discharge and poses a risk of reduction in downstream water availability. *Earth's Future*, *14*, e2025EF007809. https://doi.org/10.1029/2025EF007809

Received 27 NOV 2025
Accepted 18 JUN 2026

Author Contributions:

Conceptualization: Chengwei Wan, John J. Gibson
Formal analysis: Chengwei Wan, Chenghao Chen, Grzegorz Skrzypek
Funding acquisition: Peng Yi
Investigation: Chengwei Wan, John J. Gibson
Methodology: Chengwei Wan, John J. Gibson
Supervision: Grzegorz Skrzypek
Visualization: Grzegorz Skrzypek
Writing – original draft: Chengwei Wan, Grzegorz Skrzypek

Abstract Global warming and permafrost thaw have significantly altered landscapes and hydrological conditions in permafrost regions. While site-specific process studies have described hydrological changes during thawing, basin-scale impact assessments and streamflow modeling remain challenging due to landscape heterogeneity and complex interactions. This study introduces a space-for-time framework using thermokarst lake indicators to quantify elevation-dependent hydrological shifts driven by permafrost degradation. On the Qinghai-Tibet Plateau, findings suggest a gradual transition in precipitation-runoff regimes, with warm-season precipitation becoming increasingly delayed and increasingly contributing to cold-season runoff. Currently, continuous permafrost dominates high elevation, transitioning to discontinuous permafrost at mid-elevation and seasonally frozen ground at low elevation, a gradient expected to diminish under future climate scenarios. Water yield mirrors this zonation, originating primarily from continuous and discontinuous zones, and declining in seasonally frozen areas. As thawing progresses, the overall water yield is projected to decrease. Simulations indicate that thawed low-elevation landscapes will buffer runoff pulses from higher elevations, delaying seasonal discharge and reducing basin-scale outflow, ultimately diminishing downstream water availability. Our analysis demonstrates the primary influence of landscape connectivity in shaping runoff dynamics and biogeochemical pathways in mountain systems undergoing permafrost degradation.

Plain Language Summary Global warming is causing permafrost to thaw. This process is changing landscapes and water flow in cold mountain regions that frequently act as water towers for lowlands. To date, most thaw studies have been limited to specific sites, with limited success demonstrated in upscaling predictions to larger basin scales. This study uses a new approach that examines thermokarst lakes as indicators of shifts in water systems, capturing permafrost degradation effects across a range of different elevations. On the Qinghai-Tibet Plateau, rainfall patterns are changing: more summer rain is stored and released later, adding to winter runoff. Currently, high elevations have continuous permafrost, mid-elevations have discontinuous permafrost, and low elevations have seasonally frozen ground. This pattern will fade as the climate warms. As permafrost thawing continues, overall water supply will also decrease. Our simulations suggest that thawed lowlands will slow down water delivery from higher areas, delaying seasonal river discharge and reducing the total water reaching downstream landscapes. Implications may include less available water for ecosystems and people, especially in summer during times of high agricultural demand. This study highlights the transformative role of landscape changes on water movement and chemical processes in mountain regions affected by permafrost loss.

1. Introduction

Permafrost is a distinctive and widespread feature of high-latitude and high-altitude landscapes, which strongly controls water cycling processes and impacts terrestrial and aquatic ecosystems (Lafrenière & Lamoureux, 2019). Rapid and amplified warming over recent decades has led to widespread permafrost thaw and degradation, as evidenced by the poleward shift of the permafrost boundary, the reduction or disappearance of near-surface permafrost, and the extensive transition from continuous to discontinuous permafrost (Biskaborn et al., 2019; Jin et al., 2021). This transition has been accompanied by intensified landscape disturbances, leading to substantial alterations of hydrological regimes, particularly across Arctic and subarctic regions, for example, in

Writing – review & editing: John J. Gibson, Peng Yi, Xicai Pan, Grzegorz Skrzypek

Siberia, Alaska, and Canada (Nitze et al., 2017; Stolpmann et al., 2024; Wright et al., 2022). Significantly, shifts in hydrological regimes affect both local and regional water quantity and quality, as hydrochemical composition responds to changes in the water cycle driven by the release of stored water and carbon. These changes alter aquatic and terrestrial productivity and contribute to elevated emissions of greenhouse gases such as carbon dioxide and methane (Vonk et al., 2019).

Permafrost thawing has been widely reported across the Arctic river basins, with basin-scale impacts including increased annual river discharge, cold-season low flows, and decadal trends toward reduced streamflow variability (Bring et al., 2017; Wang et al., 2021). Unlike the low-gradient landscapes typical of high-latitude pan-Arctic, permafrost in the Qinghai-Tibet Plateau (QTP) is characteristic of high-altitude systems, whereby its distribution is strongly influenced by topography (Zhao et al., 2021). In these high-relief basins, elevation acts as a dual control of permafrost degradation and hydrological connectivity, resulting in complex and heterogeneous regional hydrology (Zhang et al., 2023). Permafrost thaw research in these mountain systems remains limited, and existing results are inconsistent. Notable examples from the QTP include studies in the Yangtze River headwaters, where increases in total discharge and baseflow have been detected (Song et al., 2021). In contrast, declining trends in total winter discharge from the Yellow River headwaters in northern QTP have also been reported (Gao et al., 2016). Due to the complex interplay of controlling factors, including permafrost temperatures, permafrost type, permafrost thaw depth, ground ice content and vegetation cover (Qiu, 2012), the cumulative impact of permafrost degradation on the hydrological response and hydrographic timing remains a topic of ongoing debate (Jin et al., 2022). Conclusions drawn from basin-scale assessments have also been inconsistent with some field-based observations, and as noted previously, cannot be reliably extrapolated to predict hydrologic responses at different spatial scales (Gao et al., 2016, 2021).

In large river basins, the streamflow hydrograph reflects the integrated contributions of runoff generation across heterogeneous landscape units. These contributions are mediated by hydrological connectivity, which governs water routing dynamics and discharge timing through coupled surface-subsurface flow pathways. The delayed hydrological responses of streamflow to permafrost thaw (Qin et al., 2025) and the spatial heterogeneity in complex basins (Sheng et al., 2020) create significant challenges in detecting basin-scale impacts. Although initial thaw generation may be similar across frozen landscape units, diverging hydrological regimes driven by rainfall, snowmelt, permafrost thaw, and runoff (Krogh & Pomeroy, 2018), lead to distinct seasonal and interannual flux dynamics. This complexity highlights the persistent challenge of scaling up point-based observations to basin-scale processes in permafrost-affected landscapes (Song et al., 2022).

Stable isotope tracers have proven effective in tracking hydrological changes in thermokarst lakes across North America, Siberia, and the QTP, revealing shifts in water balance, lake expansion, drainage cycles, and evaporative processes (Ala-aho et al., 2018a; Bouchard et al., 2016; Yang et al., 2016). However, existing large-scale syntheses (e.g., MacDonald et al., 2016; Narancic et al., 2017; Yang et al., 2021) have primarily focused on qualitative metrics, such as evaporation-to-inflow ratios, to assess lake status (shrinking vs. expanding) rather than quantifying landscape effects and actual water yield (runoff generation). While recent isotope mass balance models have addressed this quantification gap (Gibson et al., 2019; Wan et al., 2019), they have largely been restricted to local catchments or temporal snapshots, limiting their ability to reveal the full spatial-temporal evolution of water availability across large basins. Building on this approach, there is a growing opportunity to characterize the integrated hydrological responses across broader regions by coupling isotope-derived metrics with machine learning upscaling and multi-scale validation. Unlike previous studies that treated connectivity as a static binary state (Yang et al., 2019), this integrated approach has greater potential for characterization of elevation-dependent hydrological connectivity in high-relief systems. Such characterization facilitates the spatial and temporal prediction of basin-scale water yield dynamics within complex, evolving systems like the QTP, with model outputs validated against observational data (MacDonald et al., 2016). Developing representative hydrographs for permafrost thaw is analogous to constructing catchment-scale hydrographs, as it provides a foundation for more accurate prediction of future changes in water fluxes and solute transport in response to ongoing permafrost degradation (Wan et al., 2019).

In our study, 3-year field observations were conducted in the source area of the Yellow River (SAYR), northeastern QTP, between 4,100 and 4,800 m (Figure 1a; Figure S1 in Supporting Information S1). This ~700-m elevational gradient naturally encompassed a landscape transition of frozen soil types spanning from seasonally frozen ground (SFG) to extensive discontinuous, sporadic, and continuous permafrost. Eighty-four lake

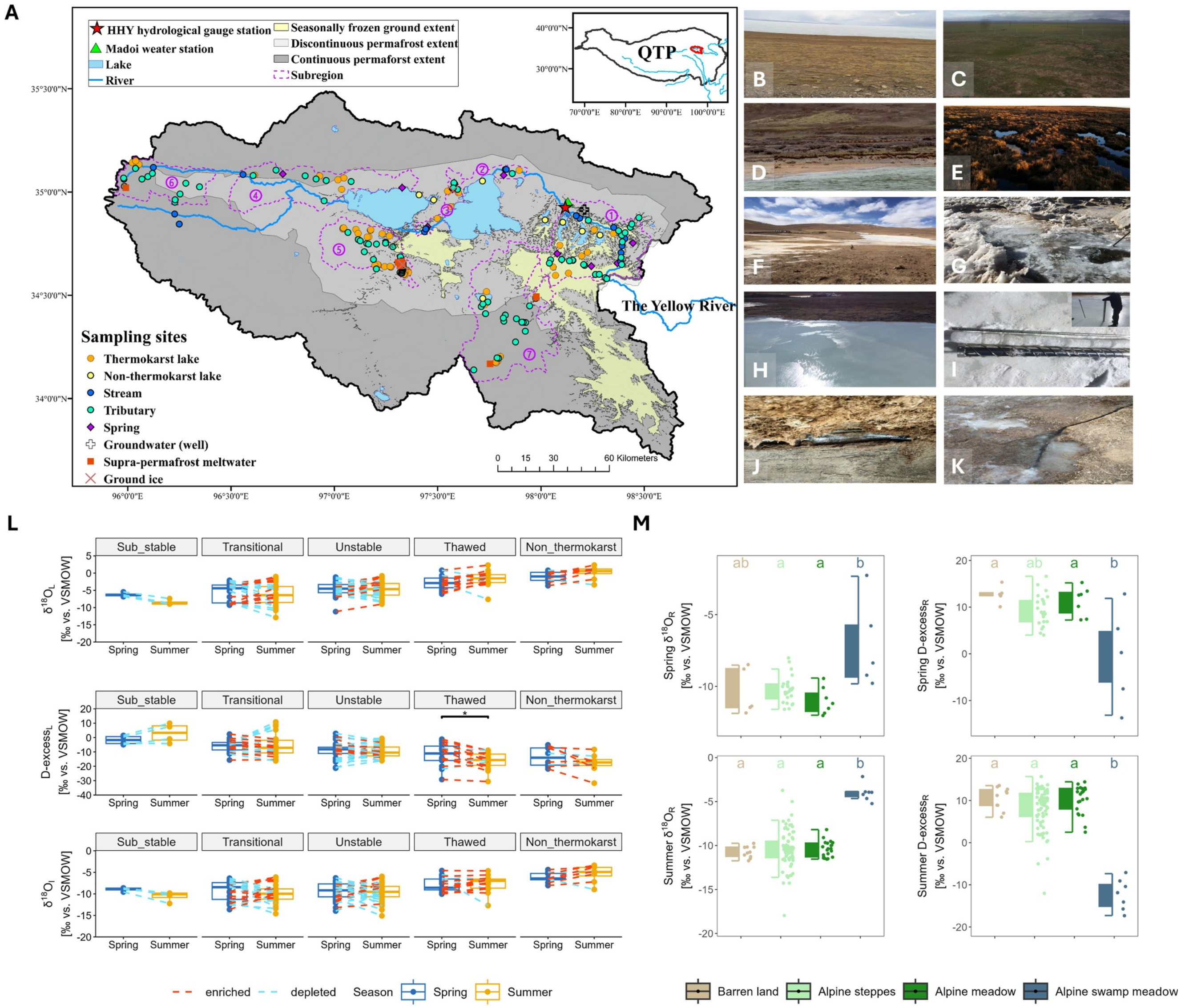

Figure 1. Map of the study area showing the 618 water samples collection points for isotope analysis in 2014–16 across seven subregions (①MD, ②ELH, ③HRQ, ④TCM, ⑤MDX, ⑥HW and ⑦CLP) within the SAYR. Permafrost distribution is based on an existing distribution data set (J. Li, 2020). Study area photos B-E depict four dominant landscape types: barren land (b), alpine steppe (c), alpine meadow (d) and alpine swamp meadow (e). Additional photos depict an ice-covered tributary in winter (f), active sub-ice flow from a hillside after drilling through surficial ice (g), an ice-covered thermokarst lake and depth-stratified sampling approach (h) and (i), water infiltrating into soil cracks to form shallow ground ice (j) and frost within the active layer in winter (k). Box plots (l, m) illustrating seasonal changes in lake water stable isotope compositions ($\delta^{18}O_L$ and d-excess$_L$) and inferred lake inflow $\delta^{18}O_I$, grouped by permafrost classification (l), and river water stable isotope compositions ($\delta^{18}O_R$ and d-excess$_R$) grouped by landcover (m). Colored dashed lines indicate spring to summer trends toward heavy isotope enrichment (red) or depletion (cyan) in $\delta^{18}O_L$. For lakes, significant differences between seasons are indicated by * ($P < 0.05$). For rivers, significant differences between groups are indicated by lower case letters ($P < 0.05$).

watersheds representing diverse landscape types were surveyed and sampled during the study (Figures 1b–1e; Figure S2 and Table S1 in Supporting Information S1). Stable isotope compositions ($\delta^{18}O$ and $\delta^{2}H$) were analysed in lakes, streams, tributaries, groundwater, ice cover, and ground ice (Figures 1f–1k), which informed an isotope mass balance model used to calculate watershed-scale hydrological indicators (Figures 1l and 1m). To address the scale mismatch inherent in earlier point-based studies, machine learning models were applied to upscale water-yield mapping, to estimate annual water yields for 1960–2014, and to generate predictions for 2046–2080 under multiple Socioeconomic Pathways (SSPs) scenarios. The primary objective of this study was to develop a conceptual framework for mapping the evolutionary trajectory of hydrological responses to permafrost thaw, using regional survey data compiled from water yield statistics, long-term gauged runoff records, and remote sensing classification of lake number and areal extent. This framework was applied to the source region of the Yellow River in the QTP to guide future efforts in acquiring relevant in situ observations and to support basin-scale mapping of permafrost-hydrology interactions in actively degrading permafrost zones. We tested whether our combined approach could provide deeper insights into large-scale catchment hydrological evolution, patterns that may be overlooked when relying solely on discrete, site-specific observations of the thaw process.

2. Data and Methods

2.1. Study Area

The study watershed, encompassing 20,930 km^2 in the northeast Qinghai-Tibet Plateau (95°55′ to 98°41′E and 33°56′ to 35°31′ N), forms the headwaters of the Yellow River (named as Source Area of the Yellow River, SAYR; Jin et al., 2009) (Figure 1a). Elevation ranges from ∼4,100 m a.s.l. In the eastern valley to ∼5,200 m a.s.l. At the summit of Mountain Bayan Har (Luo et al., 2018), with a mean elevation of ∼4,500 m. Originating in the west, the Yellow River flows eastward, sustained by numerous tributaries and small mountain creeks that converge to form a braided and meandering drainage network (Ma et al., 2023). There are four main types of vegetated landcover in the region: barren land or deserted steppe, which is distributed sparsely in eastern areas with seasonally frozen ground; alpine steppe, dominated by gramineous species, which occupies valleys and fluvial or alluvial plains; alpine meadows, which occur widely over peaty flatlands in the elevation range from 4,300 to 4,800 m, and paludal and alpine swamp meadows, which have formed on low-relief river and lake terraces (J. Li et al., 2016).

The distribution of seasonally and permanently frozen soil is governed by a range of complex factors, including elevation, topography, hydrogeology, local climate zonation, and the presence of water bodies. While local landforms such as slope aspect and vegetation cover influence ground thermal regimes (J. Li et al., 2016), elevation acts as the dominant first-order control determining permafrost presence in this high-relief region (4,200–5,000 m). Consequently, this study utilizes elevation bands as a primary zoning metric to capture the vertical gradient of permafrost stability. Frozen ground covers 80% of the entire study region. Based on the MAGT range, we classified four distinct levels of permafrost stability in this study: sub-stable (−3.0 ∼ −1.5°C), transitional (−1.5 ∼ −0.5°C), unstable (−0.5 ∼ 0°C), and thawed (>0°C, seasonally frozen ground) (Ran., 2019). Permafrost in SAYR is relatively warm (>−2.0°C), thin (<100 m), ice-rich, with high ice content near the permafrost table. It is thermally unstable and therefore highly vulnerable to climate warming. This vulnerability creates a complex mosaic of different permafrost landscapes, with frequent transitions between the continuous, discontinuous, sporadic, and isolated permafrost zones, as well as areas of seasonally frozen ground (J. Li et al., 2016). The active layer thickness varies between 0.6 and 3.0 m, and it is attributed to a diversity of spatial thermal regimes under vegetation and peat substrates (Luo et al., 2018). High ground-ice content of plains and platform deposits, and the collapse of ice mounts and pingos caused by permafrost degradation since the 1970s, have promoted the development of thermokarst lakes as well as taliks (Jin et al., 2009).

2.2. Long-Term Meteorological and Hydrological Lake Attributes

Spatially continuous ERA5-Land reanalysis data provided the primary inputs for the Isotope Mass Balance (IMB) model and basin-scale hydrological analysis. Daily meteorological data (air temperature, precipitation and potential pan evaporation rates) were obtained from the Madoi Meteorological Station (98.08°E, 34.57°N) for the 1956–2016 period. These data were solely for the validation and assessing the reliability of the gridded products. Daily discharge of the Yellow River was available from the HHY gauge station for the 1956–2016 period (the Yellow River Conservancy Commission). Data from the post-1998 period were not analyzed due to upstream hydropower station construction that influenced natural hydrological processes (Ma et al., 2019). Lake distribution data for the Tibetan Plateau (1995–2015) were extracted for lake attributes from Spatial distribution maps of lakes over the Tibetan Plateau (Observational & Geospatial, 2018). Seasons were classified as: March to May for spring, June to August for summer, September to November for autumn and December to February (the following year) for winter.

2.3. Field Sampling

Four field campaigns (16 April–6 May 2014, 14 July–15 August 2014, 24 January–2 February 2015 and 8–16 May 2016) were conducted across seven subregions (MD, ELH, HRQ, TCM, MDX, HW and CLP)

(Figures 1a) and 76 thermokarst lakes and 8 non-thermokarst lakes, representing different permafrost stability and landcover types, were sampled (Table S1 in Supporting Information S1). Thermokarst lakes acted as terminal basins, receiving defined, channelized inflows, such as small creeks from their catchments. Non-thermokarst lakes typically acted as headwater lakes with defined outlet channels, except for Ngoring (ELH) and Gyaring (ZLH) lakes, which were throughflow systems. All 84 lakes were visited in two seasons, spring and summer of 2014; 4 lakes were resampled in 2015, and 27 lakes were resampled in 2016.

In total, 14 individual samples of rain and snow were collected (Figure S3 and Table S2 in Supporting Information S1). Surface, subsurface water, and ice samples were collected from spatially distributed sites during targeted sampling campaigns. In total, 203 lake water samples and 189 stream and tributary river water samples were obtained. The samples were collected ∼0.5–1.0 m from the lake/river shore at a depth of 0.2–0.3 m below the water surface, assuming that the lake and river waters were well mixed and unstratified. In addition, 13 springs were sampled, and 22 deep-bore samples were collected in small towns in the central eastern part of SAYR. Fourteen supra-permafrost thaw samples were collected using a vacuum pump to extract from the upper permafrost ice layer (∼3 m deep) during on-site borehole-drilling in the warm summer season (July–August 2014) (Table S2 in Supporting Information S1). Additionally, 26 near-surface ground ice samples, extending to a depth of 3 m, were collected through mechanical drilling from evacuated permafrost profiles in the spring season (April 2014). In winter (January–February 2015), 4 lake ice cores and 7 river ice cover cores, and shallow frost samples were obtained using a specially designed corer and sectioned into 10-cm subsamples (Figures 1f–1i). Subsequently, sub-ice water was collected from augured holes at the center of lakes to capture the baseflow conditions (Table S3 in Supporting Information S1).

Liquid water samples were stored at 4°C in 20 mL high-density polyethylene bottles without headspace, tightly sealed with parafilm to minimize evaporation. All ice samples were preserved frozen until analysis.

2.4. Stable Isotopic Analysis and Isotope Mass Balance (IMB) Modeling

Stable hydrogen and oxygen isotope analyses were carried out in 2017 at InnoTech Alberta, Victoria Canada, using established IRMS methods. For δ^2H, a PAL autosampler (CTC Analytics AG, Zwingen, Switzerland) injected 1 μL of H_2O into an HDevice containing chromium metal at 875°C to produce H_2 gas from H_2O, which was then introduced to the IRMS (Brand et al., 1996). For δ^{18}O, a GasBench II peripheral was interfaced with the IRMS, where H_2O was placed in sealed vials flushed with 0.3% CO_2 in helium, allowing oxygen in H_2O to exchange with oxygen in CO_2 gas (Nelson et al., 2008). Multiple CO_2 portions were introduced into the IRMS via the autosampler for analysis of stable oxygen isotope composition against a pure CO_2 reference gas (Paul & Skrzypek, 2006). Analytical uncertainty was ±0.8‰ for δ^2H and ±0.1‰ for δ^{18}O (1 standard deviation) based on replicates. Results are reported as 1000 isotope delta values in permil (‰) relative to Vienna Standard Mean Ocean Water (VSMOW, δ^2H 0‰ and δ^{18}O 0‰) and normalized on the VSMOW/SLAP scale (Standard Light Arctic Precipitation δ^2H −428.0‰ and δ^{18}O −55.5‰) after multi-point normalization to laboratory standards (Figure S4, Tables S2 and S3 in Supporting Information S1).

2.5. Isotope Mass Balance (IMB)

The isotope mass balance (IMB) model was applied to describe the site-specific hydrology of lakes. This approach has been described in detail before and is widely used in thaw and non-thaw lakes (Gibson et al., 2016; Narancic et al., 2017). The basic assumption is that evaporated waterbodies tend to plot along a lake-specific evaporation line (LEL) defined by lake water isotope compositions (δ_L), which is regulated both by input sources of precipitation/runoff (δ_I) and potential for enrichment under prevailing atmospheric conditions to a limiting isotopic composition (δ^*) (Figures S5 and S6 and Table S4 in Supporting Information S1).

$$\mathrm{x} = \mathrm{E}/\mathrm{I} = (\delta_I - \delta_L)/(\delta_E - \delta_L) \tag{1}$$

δ_I is the average isotope composition of source water, which is estimated using the coupled isotope tracer method introduced by Yi et al. (2008). δ_I is recognised to be the point of intersection between a LEL and the local meteoric water line (LMWL). δ_E is the isotopic composition of evaporated water:

$$\delta_E = \left(\left(\delta_L - \varepsilon^+\right)/\alpha^+ - h\delta_A - \varepsilon_K\right)/\left(1 - h + \varepsilon_K \times 10^{-3}\right)\ (‰) \tag{2}$$

10.1029/2025EF007809

where h is the relative humidity, δ_A is the isotopic composition of atmospheric moisture, ε^+ is the equilibrium isotopic separation (Horita & Wesolowski, 1994), α^+ is the equilibrium isotopic fractionation, where $\varepsilon^+ = \alpha^+ - 1$, and ε_K is the kinetic isotopic separation (Horita et al., 2008).

$$\delta_A = \left(\delta_P - \varepsilon^+\right) / \alpha^+ \tag{3}$$

A total number of 175 event-based precipitation samples (snow and rain), collected during May 2009–May 2010 and reported by Ren et al. (2013), were used to establish the LMWL and to estimate the amount-weighted average precipitation isotopic composition (δ_P). In addition, rainfall and snow samples collected during this study were analyzed to evaluate the LMWL and to compare seasonal precipitation isotope characteristics with previously reported data (Figure S6 in Supporting Information S1).

In our study (Figure S6 in Supporting Information S1), the average isotope composition of source water δ_I is assumed to originate from atmospheric precipitation and is assumed to fall along the LMWL (i.e., soil water active layer, shallow groundwater, snowmelt). Source water originates mainly from permafrost thaw water with low delta values (e.g., resulting in δ_L plotted above LMWL) (Figure S4B in Supporting Information S1), therefore, the calculation of δ_I according to Yi et al. (2008), would introduce some bias and uncertainties in E/I estimates. Thus, using δ_I estimated from the intersection between a LEL and the permafrost meltwater line could be regarded as a more reliable approximation (Figure S5 in Supporting Information S1).

Considering that

$$I = P + R \tag{4}$$

where P is the precipitation that falls onto the lake surface and R is the ungauged flow from the watershed.

R can be estimated if the evaporation is known:

$$R = E/x - P\left(\mathrm{m}^3\right) \tag{5}$$

where $E = e \cdot \mathrm{LA}$ and $P = p \cdot \mathrm{LA}$; e and p are the annual evaporation and precipitation (m), and LA is the lake area (m^2). So, water yield (WY) can be estimated as:

$$WY = R/DBA \cdot 1000\ (\mathrm{mm}) \tag{6}$$

where DBA is the drainage basin area of the individual lake (m^2), $DBA = WA - LA$, and WA is the watershed area of each lake (m^2). The runoff ratio is defined as WY (mm)/P (mm).

Samples for determining δ_L values were collected in mid-late April, when lake ice is nearly absent, and local water evaporation is negligible (<1 mm/d), and were assumed to represent conditions from the preceding hydrological year. These values reflect the lake water isotope compositions modified by the recharge (including snow on the lake surface in the ice-on season) and evaporation during the open-water season over the preceding hydrological year since the lake became ice-free. E/I estimated from δ_L values sampled during spring and summer seasons were subsequently used to model the runoff metrics at two scales: (a) annual, covering the period from ice cover melt in 2013 to sampling date in 2014, and (b) seasonal, representing spring-summer ice-free period in 2014. Additionally, δ_I estimates and related metrics were applied to 2016 lake samples for data validation using our machine learning algorithms.

2.6. Secondary Data Processing

Watershed areas (WA) for each sampled lake were delineated using Whitebox Tools (Lindsay, 2016; *R* package) based on a 30-m digital elevation model (DEM) and outlet point shapefile. Each watershed was defined as a drainage basin with the lake positioned as the downstream outlet (Gibson et al., 2018). The delineated watershed boundaries were further validated using high-resolution Google Earth imagery (Google, n.d.), drone-based aerial photographs, and 1:250,000 geological and environmental maps compiled for the SAYR between 2001 and 2004.

Gridded ERA5-Land reanalysis climate parameters, including air temperature, relative humidity, precipitation, and potential pan evaporation rates, were used as primary inputs for IMB modeling and were supplemented with post-processed daily statistics (Table S4 in Supporting Information S1). These daily climate variables covering 2013–2016, were interpolated to $0.1° \times 0.1°$ grid cells corresponding to each lake (Copernicus Climate Change Service, Climate Data Store, 2024). Daily evaporation rates were also used to calculate flux-weighted estimates of air temperature and relative humidity, improving the simulations of lake water evaporation during each period (Gibson et al., 2019). This data set was selected based on recent comparative assessments conducted in high-altitude regions (Yang et al., 2024), which demonstrated that ERA5-Land outperforms satellite precipitation products in capturing solid precipitation and multi-year discharge variability in the QTP. Our local validation against the Madoi station records confirmed that ERA5-Land successfully reproduced regional climatic patterns and interannual variability.

2.7. Machine Learning Model Performance and Transparency

Machine learning (ML) models have demonstrated strong capability in simulating complex hydrological systems and capturing the complex non-linear relationships among multiple input and output variables. When combined with SHapley Additive exPlanations (SHAP), these models offer interpretable insights into the relative influence of different drivers on water stable isotope composition and hydrological indicators (details see Text S1 in Supporting Information S1). Prior to modeling, we performed variable selection using the correlation analysis, variance inflation factor (VIF) method and the Boruta algorithm to minimize multicollinearity, reduce overfitting and identify the most relevant predictors (Figures S7 and S8 in Supporting Information S1). The Topographic Wetness Index (TWI) variable was found uninformative and was excluded from future analyses.

A total of 16 predictor variables, classified into four main groups (climate, landscape, topography and permafrost), were used as independent inputs (Text S1 and Table S6 in Supporting Information S1). The dependent targeted variables included annual water yield (WY), summer WY, post-summer runoff fraction, annual WY/P, annual evaporative-to-inflow ratio (E/I), annual inferred lake inflow δ^{18}O ($\delta^{18}O_I$), summer $\delta^{18}O_I$, spring and summer river δ^{18}O ($\delta^{18}O_R$) and d-excess (d-excess$_R$). Machine learning model and SHAP analyses were conducted using ensemble-stacked models implemented via the updated "h2o" package (v3.46.0.7) in the R programming language platform (details see Text S1, Fryda et al., 2023). This ensemble approach inherently reduced the variance of individual base learners, preventing the model from fitting to local noise and ensuring better generalization across the heterogeneous landscape.

2.8. Annual Water Yield Mapping and Regional Upscaling

Based on the machine learning modeling results (Table S8 in Supporting Information S1), we found that annual water yield could be well explained by the selected factors, with WA having negligible influence on annual WY prediction (Figure 3a). To better delineate the temporal and spatial effects of the annual water yield changes, we applied grid-based interpretable machine learning. The model was retrained using all variables excluding soil water content, evapotranspiration and watershed area and achieved reliable performance results both on training ($R^2 = 0.93$) and validation ($R^2 = 0.77$) sets (Figures S9 and S10 in Supporting Information S1). In the context of regional hydrological upscaling, this result confirmed the model's robustness and its suitability for basin-wide simulations. We set the grid resolution to 450 m (equal to ~0.2 ha) and resampled all related variables (annual averages) from multiple grid-based data sets (Tables S6 and S9 in Supporting Information S1) to this resolution. Ensemble models were then applied to upscale past annual water yield changes at the regional scale (for each year from 1961 to 2014). The time-series of annual average values of these variables were also extracted, whenever possible, except for topography features, Vegetation_coverage, ground_ice, and Instability_index. To predict annual water yield changes in the future at the regional scale under different SSPs (SSP1-2.6, SSP2-4.5, and SSP5-8.5) scenarios, we extracted annual air temperature, precipitation, MAGT, ALT and permafrost coverage data from different general circulation models (GCMs) (Table S9 in Supporting Information S1). Open water bodies were masked from the annual WY maps. Uncertainty in the historical WY estimates (1961–2014) was calculated as ±1 standard deviation around the mean predictions of base models. For future WY predictions (2046–2080), annual WY was estimated as the mean output from models driven by annual temperature and precipitation data inputs from 17 different GCMs (Table S9 in Supporting Information S1), with uncertainty quantified as the standard deviation of the different models.

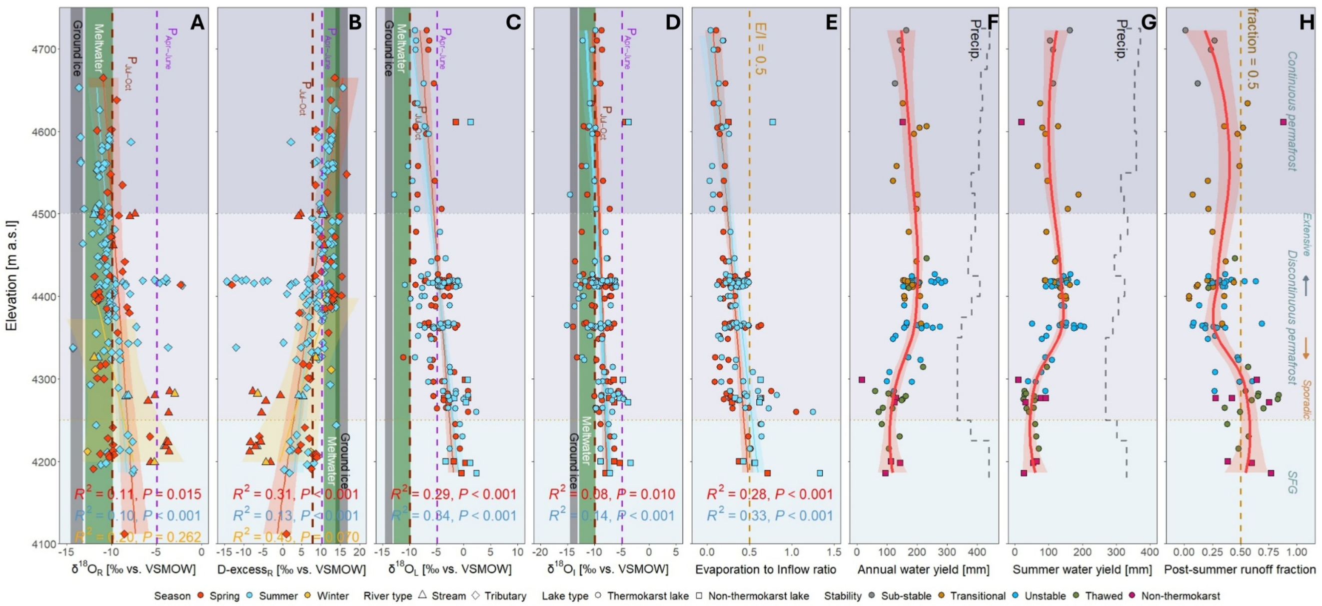

Figure 2. Elevation gradients of key hydrological and isotopic indicators in the study area. Panels show river water $\delta^{18}O_R$ (a), d-excess$_R$ (b), lake water $\delta^{18}O_L$ (c), inferred inflow $\delta^{18}O_I$ (d), estimated evaporation to inflow ratio (E/I) (e), annual water yield (WY) (f), spring-summer water yield (g) and post-summer runoff fraction (h) in the study area. Transition of frozen soil types along elevation gradients is also noted (h). For panels (a–e), colors of points represent seasons, shapes represent river and lake types; purple and brown dashed lines show average isotopic value of precipitation in April–June and July–October, respectively; green and gray bars show ranges of isotopic compositions in permafrost meltwater and deep ground ice, respectively. Solid line with shades illustrating linear regression and 95% CI between elevation and water isotopic compositions, R^2 and significance values are also labeled and color-coded by season. For panels F-H, colors of points represent permafrost stability of lake watersheds, shapes refer to lake types; the red lines and shades represent the smoothed values; derived using the loess function as implemented in R (R Core Team, 2023). Stepped dashed lines in F and H indicate average annual and spring-summer precipitation amounts across 50-m elevation gradient intervals in SAYR, respectively.

2.9. Statistical Analyses

Trends in climate and hydrology variables were analyzed using the nonparametric Mann-Kendall test and Theil-Sen's slope analysis, with trend-free pre-whitening to remove serial correlation in the data (Jiang et al., 2017; Yue & Wang, 2002). Linear regressions were also used to evaluate relationships between monthly discharge and precipitation for each study period.

Statistical comparisons of stable isotope compositions and hydrological indicators were conducted across water-source categories, grouped by watershed landscape and permafrost stability. Due to the lack of normal distribution or equal variances at 95% confidence level ($P < 0.05$), Kruskal-Wallis one-way analysis of variance (ANOVA) analysis and Dunn's post-hoc test with Bonferroni-adjusted significance values were applied to perform pairwise multiple comparisons. Linear relationships between multiple catchment attributes, environmental conditions, and permafrost-related parameters were assessed by using the Pearson correlation coefficient. All statistical analyses were performed using *R* v4.2.3 (R Core Team, 2023).

3. Results and Discussions

3.1. Modern Permafrost Stable Isotope Hydrology

3.1.1. Hydrological Characteristics Along an Elevation Gradient Inferred From Stable Isotope Analysis

The correlation between the stable isotope compositions of river and lake water and elevation (Figure 2; Table S2 in Supporting Information S1) indicates elevation-dependent watershed hydrological processes. A steeper summer $\delta^{18}O$ elevation gradient in lake water reflects short-term hydrological pulses. In contrast, the reduced spring gradient suggests the smoothing effect of prolonged evaporation and overwinter hydrodynamics (Figure 2). A widespread seasonal decrease of $\delta^{18}O$ from spring to summer was found in lake water (Figure 11), demonstrating distinct hydrological responses to permafrost thaw. Sub-stable permafrost areas (>4,500 m) showed summer $\delta^{18}O$ decrease and d-excess increase, indicating recharge from permafrost thaw. Conversely,

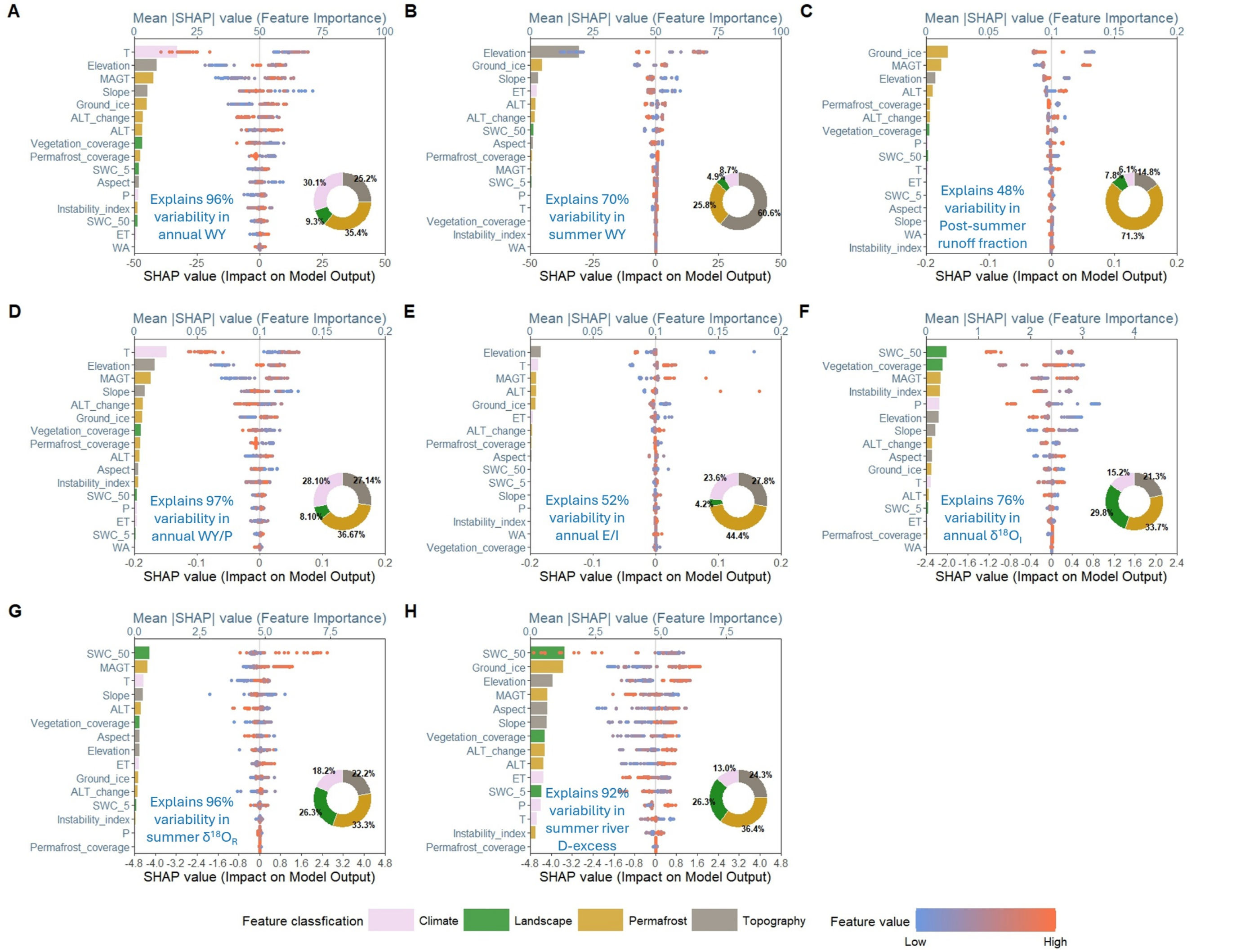

Figure 3. Feature importance and Shapley Additive exPlanations (SHAP) analysis for the optimal stacked ensemble machine learning models, illustrating influence of each test sample as colored dots on the outputs of best ensemble models: the predicting annual WY (a), spring–summer WY (b), post-summer runoff fraction (c), annual WY/P (d), annual E/I (e), inferred annual average inflow $\delta^{18}O_I$ (f), summer season river water $\delta^{18}O_R$ (g) and d-excess (h). Bar charts with a top *x*-axis show the absolute summary (mean (|SHAP value|) of the 16 selected features ranked in order of descending feature importance. Donut chart depicting the relative importance of each feature classification as a percentage of the total importance.

transitional and unstable discontinuous permafrost zones (~4,350–4,500 m) exhibited a summer $\delta^{18}O$ increase, signaling reduced thaw inputs. Thermokarst lakes showed $\delta^{18}O$ increase patterns similar to non-thermokarst lakes in SFG areas below 4,300 m, where permafrost became absent. Variations in water isotopic compositions within the hydrological system were mainly described in Text S2 in Supporting Information S1.

River water exhibited a significant elevational-dependent trend in d-excess during the spring season (Figure 2). Rather, this d-excess pattern reflects source-water heterogeneity, driven by increasing riverine interactions with lakes, wetlands and subsurface water inputs. These inputs transition from summer-autumn precipitation ($\delta P_{July–October}$) of lower d-excess to winter baseflow contribution across high and low elevations (Wan et al., 2019). Consequently, spring tributary waters exhibited low $\delta^{18}O$ values, indicative of permafrost thaw sources, accompanied by anomalously low d-excess values at elevations below 4,400 m (Figure S11 in Supporting Information S1). These values diverged from contemporaneous precipitation ($\delta P_{April–June}$), and instead aligned more closely with the isotope signature of previous summer-autumn precipitation. The amplified isotopic variability observed in both river and lake water within the transition zones (4,300–4,500 m) reflects the spatial heterogeneity of topography, permafrost conditions, land cover types, and active layer freeze-thaw process, which generates different water sources and alters surface water recharge patterns. Notably, significantly lower δ^{18}O and higher d-excess values in the mainstream were found only in transitional permafrost zones (Figure S11 in Supporting Information S1), confirming the limited and non-uniform contribution of thaw sources characterized by low δ^{18}O throughout permafrost thaw period.

Winter ice isotope profiles reveal distinct freezing regimes and hydrological connectivity (Figures S6C and S6D in Supporting Information S1). Shallow thermokarst lakes functioned as closed systems with rapid freezing and negligible groundwater input (Gibson & Prowse, 1999). In contrast, a weak δ^{18}O-depth gradient in deeper thermokrast lakes suggested equilibrium ice-water fractionation influenced by secondary water inputs. Non-thermokarst lakes displayed open-system signatures indicative of continuous sub-ice supply. Notably, lower $\varepsilon_{ice\text{-}water}$ values (Table S3 in Supporting Information S1) and steeper δ^{18}O-depth gradient in terminal lakes, compared to high-throughput lakes, point to reduced sub-ice channel connectivity in the former (Lütjen et al., 2024).

Cores from low-elevation tributaries showed equilibrium fractionation characteristic of open-system freezing, implying stable baseflow conditions (Figures S4E and S4F in Supporting Information S1) (Gibson & Prowse, 2002; Nadeau et al., 2022). Tributaries and streams situated within lacustrine alpine swamps were indicative of high δ^{18}O inflows entering the river during the middle-late freezing stage. In contrast, higher-elevation streams and tributaries exhibited systematic shifts in isotopic signatures over winter from high to low, indicating a progressive decline in baseflow discharge.

3.1.2. Lake Water Budgets Estimated Using a Stable Isotope Mass Balance Model

A stable isotope mass balance model, based on lake water stable isotope compositions, was applied to derive key watershed hydrological metrics at seasonal and annual scales (Figures S9, S10 and Table S1 in Supporting Information S1). Low evaporation-to-inflow ratios (E/I) indicated reduced evaporative losses and higher lake inflows. E/I generally decreased with increasing elevation, aligning with physical processes observed in the field (Figure 2). The water budget of low elevation lakes (<4,300 m) was evaporation-dominated during spring-summer, with 40% of lakes having E/I greater than 0.5. Positive water budgets during the post-summer period were sustained by continued inflow. Notably, 95% of lakes above 4,350 m exhibited E/I < 0.5, and a temporal lag in inflows not directly derived from precipitation was observed. The high variability in the stable isotope composition of inferred input water ($\delta^{18}O_I$) in mid-elevation lakes (4,350–4,500 m) mirrored the observed fluctuation in lake and river water (Figure 2), further supporting the presence of heterogeneous recharge patterns driven by transitional permafrost thaw. Supra-permafrost thaw sources enhanced lake throughputs in the 4,500–4,600 m range during the spring-summer period relative to annual averages. In contrast, hydrological regimes above 4,600 m were predominantly precipitation-driven, thereby moderating the dynamics of lake expansion.

As the landscape transitions from continuous permafrost at high elevations to discontinuous or sporadic permafrost at mid-elevations, and ultimately SFG at low elevations, a characteristic progression in water yields (WY) emerges (Figure 2). Sensitivity analysis (Table S5 in Supporting Information S1) further showed that these spatial patterns were robust to uncertainties in model inputs, supporting the observed "rise and fall" dynamics of thaw-source contributions across different stages of permafrost degradation. From continuous (>4,500 m) to discontinuous permafrost area (4,350–4,500 m), annual and spring-summer WY exhibited significant increases from a mean of 167 mm (range: 12–232 mm) to 199 mm (range: 129–293 mm) and from a mean of 107 mm (range: 18–187 mm) to 135 mm (range: 51–204 mm), respectively. WY declined markedly with decreasing elevation, shifting from extensive-sporadic discontinuous permafrost to seasonally frozen soils (averaging −74 and −78 mm of decrease for annual and spring-summer seasons, respectively). Below 4,300 m elevation, the annual WY of half the number of lakes was <120 mm, and the spring-summer WY only accounted for <50% of the annual WY in nearly 40% of lakes. Half of the watersheds below 4,350 m exhibited low annual precipitation-runoff ratios (R/P) < 0.36 and derived more than half of their annual inflow from post-summer runoff. In contrast, R/P > 0.36 was typical for watersheds above 4,350 m, with spring-summer runoff dominating (>50% of annual runoff) in over 90% of watersheds.

Elevation-driven hydrological shifts resulting from permafrost degradation were found to directly influence WY regimes. However, non-linear WY responses were recorded, characterized by an initial increase during early thaw stages, followed by a subsequent decline, consistent with the release of a transient pulse of stored permafrost water (Figure S11 in Supporting Information S1) (also see Wan et al., 2019, 2020; Gibson et al., 2019). Annual and spring-summer WY were markedly reduced in thawed (SFG) and non-thermokarst watersheds relative to transitional/unstable permafrost basins. An abrupt shift from post-summer to annual WY inputs was observed at elevations of ~4,300–4,350 m, signifying the transition from permafrost watersheds to SFG systems with reduced yields. This transition highlights the onset of a broader seasonal lag in watershed hydrological response, driven by permafrost degradation and its impact on hydrological conditions.

3.1.3. Physical Drivers of Watershed Hydrology

A stacked ensemble machine learning approach was employed to identify dominant environmental drivers of watershed hydrology (Table S6 in Supporting Information S1). The model demonstrated robust explanatory power, accounting for over 90% of the variance in key hydrological metrics, including annual WY, annual WY/P ratio, and summer river $\delta^{18}O$ and d-excess values. However, limitations were noted in capturing post-summer runoff, E/I ratios and spring-season river isotope composition dynamics (Figure 3; Tables S7 and S8 in Supporting Information S1).

Distinct climatic and permafrost controlling factors emerged as drivers of annual versus spring-summer WY. The modeling framework did not assume elevation as the sole driver. However, feature importance analysis revealed that although secondary factors improved model accuracy by capturing local complexity, elevation-dependent climatic and permafrost variables consistently dominated as predictors of water yield. The prominence of physical determinants over spatial coordinates confirmed that the model captures generalized mechanistic processes and effectively minimizes bias from spatiotemporal autocorrelation (Figure 3a). In contrast, spring-summer WY exhibited stronger dependence on topography-related parameters (Figure 3b). Furthermore, a divergent regulatory pattern between climatic and permafrost factors revealed a nonlinear hydrological response to climate change. Specifically, mean annual air temperature (MAAT) exerted a negative influence on annual WY, while mean annual ground temperature (MAGT) showed a positive effect. Additionally, slope gradients were found to negatively influence annual and spring-summer WY. To distinguish permafrost degradation from confounding drivers, we evaluated vertical precipitation gradients and vegetation cover. The observed linear increase in precipitation with elevation ruled out rainfall anomalies as the cause of the abrupt water yield surge at 4,300–4,500 m. Furthermore, while the decrease in vegetation density with elevation could plausibly explain the reduction of water yield at low elevations via enhanced evapotranspiration, it failed to account for the distinct rise from high elevation to the transition zone. This was corroborated by feature importance analysis, where vegetation and soil properties combined explained only 9.3% of the variance. Permafrost-related factors primarily controlled variation in the proportion of post-summer WY within annual WY (Figure 3c), although the model explained only 48% of the variance. Ground-ice content, which enhances summer thaw release, and MAGT, which regulates the storage and delayed release of summer precipitation and thaw water within the active layer, exerted opposing influences on post-summer runoff. These landscape and permafrost controls were further modulated by climatic conditions, highlighting the need for future studies to track hydrological trajectories under jointly evolving climate and permafrost regimes (MacDonald et al., 2016; Turner et al., 2014).

Stable isotope ($\delta^{18}O$) signatures of the lake (Figure 3f) and river water (Figure 3g) were primarily regulated by soil moisture content at 50 cm depth. This highlights the role of hydraulic connectivity in facilitating shallow infiltration of precipitation and supra-permafrost thaw-source contributions. The machine learning model provided more robust explanations for inferred annual $\delta^{18}O_I$ values compared to those from the spring-summer period (Tables S7 and S8 in Supporting Information S1), likely due to reduced noise from dynamic hydrological fluctuations, enhanced detection of stable isotope signatures of baseflow. Previous studies have shown that summer storm events can significantly influence the temporal stable isotope composition of baseflow (Boreux et al., 2021), which may account for weaker correlations observed during the spring-summer period. Meanwhile, slow-varying watershed-scale factors (e.g., geological properties or subsurface dynamics associated with frozen soil) likely contributed to the greater stability of our models on the annual scale.

In contrast to lake inflow, which is locally constrained by watershed architecture, summer river water isotope signatures more effectively capture contributions from seasonally integrated watershed storage, as reflected in pronounced elevation-dependent patterns. Regionally controlled factors, such as hydraulic connectivity, played a more prominent role in facilitating the transport and mixing of isotopic signatures acquired from distal sources (e.g., high-elevation areas) into river discharge, as observed in supra-permafrost runoff and talik flow (Koch

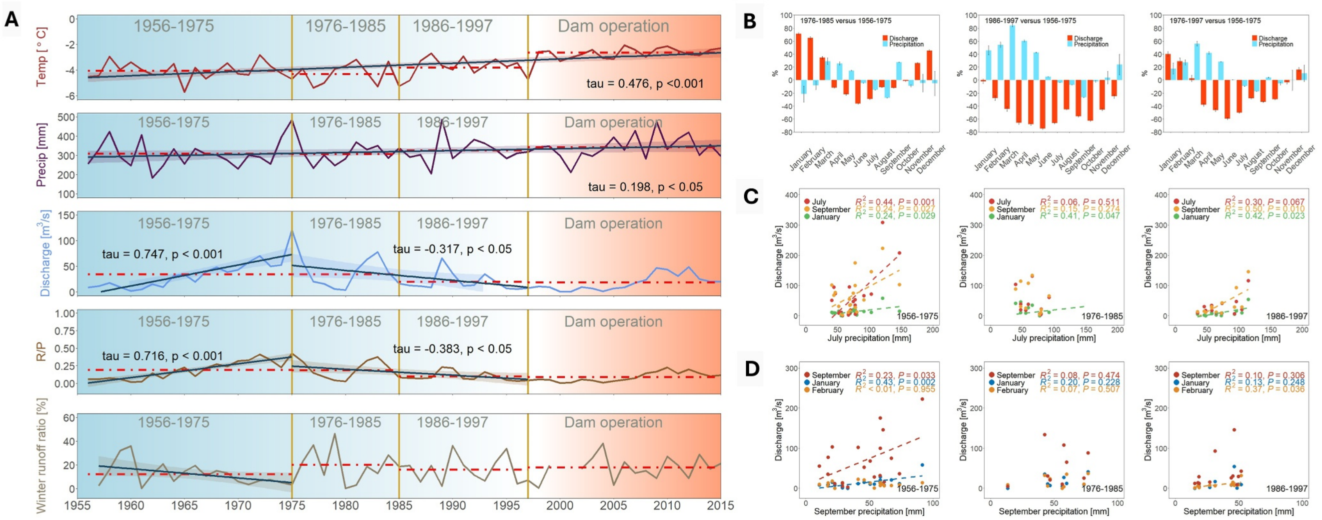

Figure 4. Long-term climate and streamflow dynamics in the SAYR. (a) Annual 1956–2015 records of mean air temperature, total precipitation, mean discharge, runoff ratio and winter runoff ratio observed at the Madoi weather station (SAYR) and hydrological station (HHY) outlet. Trends were assessed using Mann-Kendall tau statistics, with associated p-values indicating statistical significance. (b) Monthly discharge and precipitation relative to 1956–1975 observations (expressed as percentages) for 1976–1985 (left panel), 1986–1997 (middle panel) and 1976–1997 (right panel). Bars represent Mean Standard Errors. (c) Linear regressions illustrate the correlation between July, September, and January discharge and July precipitation for 1956–1975 (left panel), 1986–1997 (middle panel), and 1976–1997 (right panel). (d) Linear regressions illustrate the correlation between September, January, and February discharge and September precipitation for 1956–1975 (left panel), 1976–1985 (middle panel), and 1986–1997 (right panel). Discharge data are from HHY hydrological station on the Yellow River; precipitation data are from Madoi weather station.

et al., 2024). The combined effect of temporal runoff integration and spatial mixing likely diminished the explanatory capability of the machine learning model in predicting spring river isotopic compositions using local parameters, an expected upscaling effect.

3.2. Past Changes in the Basin Hydrology

3.2.1. Long-Term Changes in QTP Hydrographs

Gradual permafrost degradation, confirmed by multiple field observations, began no later than in the 1980s, coinciding with a significant rise in mean annual air temperature (+0.33°C/decade, $p < 0.001$) alongside a rise in precipitation (+10.44 mm/decade, $p < 0.05$) between 1956 and 2015 (Figure 4a). The annual streamflow hydrographs mirrored the observed WY dynamics along permafrost degradation gradients, exhibiting a prominently rising trend during 1956–1975 (+3.36 m^3/s per year, $p < 0.001$), followed by a persistent decline until 1997 (−1.03 m^3/s per year, $p < 0.05$), despite increasing precipitation. Average annual discharge during the initial rising phase was notably higher than during the subsequent declining phase, despite lower precipitation in the earlier period. This inverse relationship indicates that rainfall was not the primary driver of WY; instead, the observed "stair-step" discharge pattern was modulated by cryosphere processes.

Seasonally, spring-early summer (April–June) runoff was the primary driver of the initial discharge increases observed in 1956–1975. In contrast, monthly streamflow from April to November during 1976–1997 declined by ∼3.5%–59.1% relative to the earlier period (1956–1975), despite a concurrent reduction in precipitation occurring only in July, August, and October (by ∼5.3%–17.3%). Conversely, winter runoff (December–February) increased by ∼16.3%–40.1%, accompanied by a corresponding rise in winter precipitation (Figure 4b). Despite intensified snowfall (+10.4%–27.4%), winter baseflow discharge was likely limited by frozen surface conditions, with much water expected to be released in the following spring. Notably, between 1976 and 1985, monthly streamflow from November to February increased substantially by ∼26.2%–71.5% compared to the 1956–1975 period, even as precipitation declined by 4.4%–21.2% (Figure 4b). This statistical decoupling, where runoff increased despite reduced precipitation, confirmed that the excess water originated from internal storage release (ground ice melt).

The relation between precipitation events and monthly streamflow discharge evolved, exhibiting a strengthening time-lagged effect (Figures 4c and 4d). During 1956–1975, July streamflow showed a strong correlation with concurrent precipitation ($r^2 = 0.44$, $p < 0.01$), while September streamflow was weakly correlated with its precipitation ($r^2 = 0.23$, $p < 0.05$) but had a greater influence on January streamflow ($r^2 = 0.43$, $p < 0.01$) (Figures 4c and 4d). In the 1976–1985 period, the correlation between July and September streamflow and their respective precipitation became insignificant (Figure 2c), while January runoff showed a positive correlation with July precipitation. By 1986–1997, the correlation between monthly runoff and concurrent precipitation had further weakened. Notably, July precipitation exerted a more prominent influence on both September and January streamflow ($r^2 = 0.50$ and 0.42, respectively; $p < 0.05$) (Figure 4c). Additionally, the lagged effect of September precipitation extended further, showing a significant positive correlation with February runoff, whereas previously it had been linked to January runoff (Figure 4d).

The time-lagged effect of warm-season precipitation contributed to runoff during cold seasons, increasing the proportion of winter discharge within the annual streamflow. This pattern suggests a basin-scale shift in the precipitation-runoff regime. Across the two sequential periods, 1956–1975 and 1976–1997, the streamflow hydrograph progressively flattened, despite relatively unchanged intra-annual precipitation distributions (Figure S13 in Supporting Information S1).

3.2.2. Temporal Dynamics of Lake Distribution Across the Elevation Gradient on QTP

Changes in both the number and surface area of lakes larger than 1 ha were quantified across the entire SAYR region during the period 1995–2015 (Figure S14 in Supporting Information S1). Satellite monitoring revealed an overall increase during 1995–2015: lake inventories grew from 1,288 to 1,517 water bodies, with total surface area rising from 1,416 km^2 to 1,484 km^2. Most lakes below 4,300 m experienced area shrinkage between 1995 and 2005, whereas lakes above 4,300 m expanded rapidly from 2005 to 2015. Over these two decades (Figure S4A in Supporting Information S1), both lake abundance and surface area increased above 4,300 m, primarily driven by the proliferation of newly-formed small lakes (1–10 ha). These changes reflect a transition in dominant hydrological drivers, from warming-induced evaporative shrinkage to expansion driven by permafrost thaw, which aligns with the elevational gradient of the E/I ratio.

Lake responses exhibited tripartite elevation dependence. Below 4,300 m within the SFG zone, evaporative shrinkage was the dominant process, driven by atmospheric warming. A comparative analysis of individual lakes larger than 10 ha revealed that 34 lakes degraded or disappeared from 1995 to 2005, with an additional 14 lakes lost during the 2005–2015 period (Figure S4C in Supporting Information S1). The abundance of small lakes (1–10 ha) increased during the first decade (1995–2005) but then declined in the second decade (2005–2015), resulting in a minimal net change. Conversely, the total surface area of medium-to-large lakes (100–10,000 ha) initially declined, followed by partial recovery, ultimately resulting in a net overall reduction.

Extensive lake expansion driven by permafrost degradation peaked between 4,300 and 4,500 m (Figure S4C in Supporting Information S1). All lake size categories exhibited areal growth in this zone, where discontinuous permafrost predominates. Statistically significant shifts ($p < 0.05$) in area change rates were observed above 4,500 m between the two periods, 1995–2005 characterized by shrinkage and 2005–2015 marked by expansion (Figure S4C in Supporting Information S1). Areal growth was predominantly driven by the formation and enlargement of small lakes (1–10 ha). During the earlier period (1995–205), initial thaw source contributions were insufficient to offset enhanced evaporation, resulting in slight reductions in lake surface area. These lake water balances appeared highly susceptible to short-term climatic fluctuations, particularly changes in precipitation.

3.2.3. Simulated SAYR Water Yields

The machine learning model, informed by multiple data sources, was applied to estimate the annual WY at the grid scale from 1961 to 2014 (see Methods and Text S1 and Table S5 in Supporting Information S1). The results revealed a temporally stable mean annual WY at the basin scale over the past five decades, despite interannual variability at the grid scale. These estimates aligned well with the observed discharge records and lake inventory changes (Figure 5a). The elevational distribution of simulated annual WY underwent a significant transformation (Figure 5b), characterized by a pronounced rightward shift, signifying a migration of higher WY values toward higher elevations. This pattern reflects the decadal-scale hydrological impacts of permafrost degradation, as thawing progressively transformed watersheds into higher runoff-generating landscapes, consistent with findings by Connon et al. (2014).

10.1029/2025EF007809

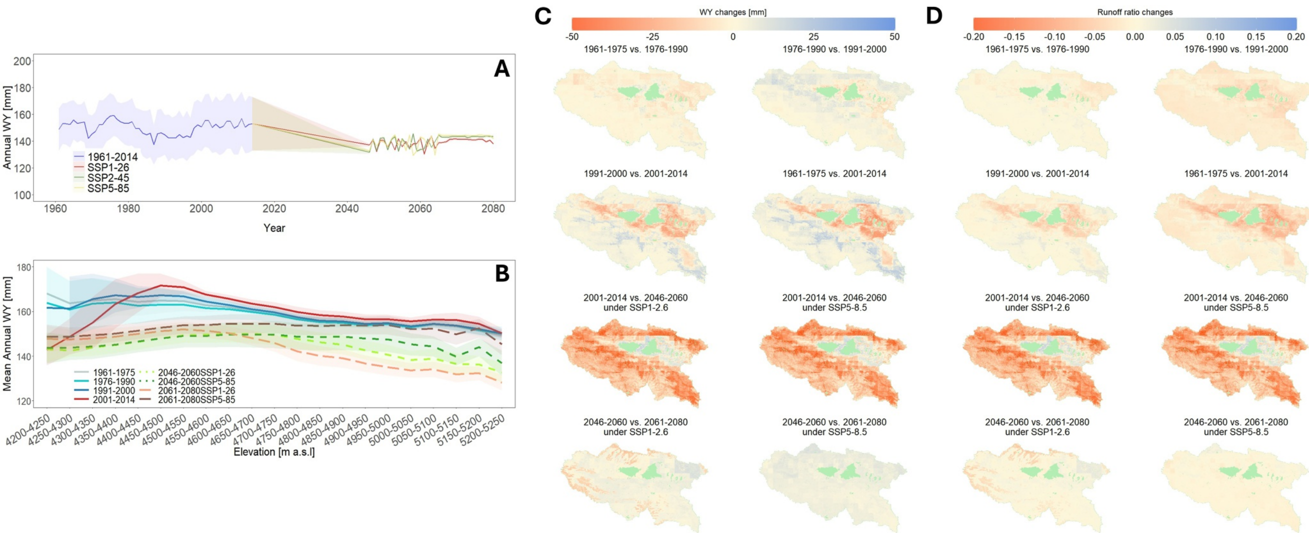

Figure 5. Historical simulations and future projections of water yield in the SAYR. (a) Simulated mean annual water yield during 1961–2014 and projected mean annual water yield for 2046–2080 under three Shared Socioeconomic Pathways (SSP) scenarios. (b) Periodic variations in mean annual water yield across 50-m elevation gradient intervals in the past and in future under different SSP scenarios. (c) Maps illustrating predicted changes in annual water yield and precipitation-runoff ratios across different periods.

The model provided a physically consistent interpretation of the long-term stability in discharge patterns at the basin outlet following the initial onset of permafrost thawing. WY, linked to early stages of permafrost degradation in low-elevation zones, appears to have directly mediated the observed increase-decrease response. Specifically, initial thaw enhanced WY in low-elevation areas during 1961–1975, followed by a progressive decline. This dynamic helped offset pronounced reductions in WY below 4,300 m, including low-lying river valley plains characterized by SFG.

The temporal evolution of WY since the 1990s has been characterized by increases primarily within the 4,300–4,700 m elevation band, with peak WY distributions shifting upward from 4,400 m to 4,500 m after the 2000s. More complex WY responses were noted in higher elevation zones underlain by continuous permafrost, where runoff ratios remained relatively unchanged despite increases in WY. Across all elevational zones of the basin, runoff ratios showed a consistent and persistent decline (Figure 5d). As permafrost degradation advanced into higher elevation zones, the onset of enhanced runoff generation became increasingly delayed, likely due to extended hydrological travel times and more intricate subsurface connectivity. These factors play a regulatory role in shaping the behavior of large river systems, consistent with observations reported by Bring et al. (2016).

3.3. Future Basin-Scale Water Yield Changes

Machine learning simulations projected divergent WY trajectories under different SSP scenarios (Figure 5a; Table S9 in Supporting Information S1). While basin-scale average WY values showed negligible differences across scenarios, substantial variation was observed in predicted interannual variability. By mid-century (2046–2060), WY is projected to decline by ∼10% relative to the 2001–2014 baseline (Figure 5a). However, by late century (2061–2080), mean WY is predicted to increase under all scenarios by 1.2% under SSP1-2.6%, 3.2% under SSP2-4.5%, and 3.3% under SSP5-8.5. SSP1-26 yielded nearly 5 mm lower annual WY, than both SSP2-45 and SSP5-85 during the late-century period, highlighting the effect of intensified global greenhouse gas impacts on this high-altitude permafrost region.

Mid-century projections were mainly characterized by WY reduction across basin-wide grids, except central, low-elevation river valleys (Figure 5c), where the peak WY elevation was predicted to ascend to 4,700–4,800 m (Figure 5a). All SSP scenarios demonstrate comparable impacts for areas below 4,750 m, while SSP5-85 predicted significantly higher WY above this elevation. These findings underscore how differential thaw rates shape water availability patterns across permafrost landscapes, with high-emission scenarios amplifying water yield increases, particularly at high elevations.

Scenario divergence becomes more pronounced in the late-century projections. Under the low-emission sustainable pathway (SSP1-26) WY was projected to increase more substantially below 4,650 m compared to the mid-century, while WY gains at high-elevation regions were suppressed (Figure 5b). Conversely, the higher emission scenario (SSP5-85) elevated WY across all elevations, with the peak yield zone shifting upwards to 4,900 m. This pattern aligns with intensified surface flow contributions and short-term WY increases, despite the associated risk of long-term water resource depletion (Wang et al., 2023).

Progressively delayed runoff responses to precipitation and thaw source inputs were confirmed by the modest changes in WY and the diminishing elevational disparities across scenarios. In the Mid-century projections, runoff ratios exhibited spatial heterogeneity (Figure 5d), increasing in northern high elevation zones despite declining WY. At the same time, late-century reduction in runoff ratios at high-elevation areas under the low emission scenario (SSP1-26) suggested a long-term shift from water-release to water-storage (Han & Menzel, 2024). Meanwhile, despite increased WY, the high-emission scenario (SSP5-85) maintained basin-wide stability in runoff ratios. This pattern may indicate a future trend toward a flattened basin-scale hydrograph, driven by altered runoff timing and storage dynamics.

3.4. Conceptual Model of Elevation-Dependent Hydrological Transition From Thawing Permafrost to Seasonally Frozen Ground

We developed a catchment-scale conceptual model to quantify elevation-dependent hydrological shifts during permafrost degradation by synthesizing multi-decadal runoff records, lake inventory dynamics, isotopic tracers, and machine learning projections. This process-based framework reveals distinct seasonal hydrological responses, contrasting summer and winter hydrological dynamics, between the early and late phases of permafrost thawing, characterized by seasonally frozen ground. It further illustrates how thaw-induced landscape reorganisation has progressively altered regional hydrological connectivity over time (Figure 6).

Early-mid degradation stage: Air temperature-driven permafrost thaw initiates thermokarst development, forming landscape depressions that promote water accumulation, illustrating the progressive alteration of flow paths as the thaw front shifts upward (Figure 6a). In low-elevation areas, WY increases disproportionately due to deeper active-layer thaw (Jin et al., 2009), although limited ground-ice content constrains abrupt runoff surges from thaw events (Guo et al., 2025; Figures S1B and S1C in Supporting Information S1). Structurally connected drainage networks facilitate short-term runoff connectivity, particularly within the active layer, channeling infiltrated thaw sources toward SFG valley floodplains (Koch et al., 2024). Enhanced subsurface storage capacity and alluvial topography amplify groundwater drainage efficiency, contributing to pronounced discharge increases (Figure 6b). However, the formation of river and lake ice in late autumn imposes thermal-hydraulic constraints on water movement, impeding recharge from surface slope runoff (Streletskiy et al., 2015). Additionally, expanded active-layer storage and features such as frost mounds, which sequester summer-autumn precipitation, reduce post-summer contributions to the annual discharge (Zhang et al., 2019). As a result, post-summer WY contributes only marginally to annual discharge regimes.

Mid-late degradation stage: Degradation of high-elevation, ice-rich permafrost triggers elevated water yields comparable in magnitude to earlier low-elevation responses; however, the limited spatial extent of these high-altitude zones constrains their downstream hydrological impacts (Figure 6b). Complete permafrost loss in mid- to low-elevation areas shifts hydrological control toward SFG regimes, amplifying hydro-ecological volatility (Figure 6a). Post-thaw terrain fragmentation creates infiltration hotspots (Şerban et al., 2021), while supra-permafrost flow pathways weaken the direct precipitation-runoff relationships (Bouchard et al., 2016), often resulting in flattened and delayed hydrograph peaks (Figure 6c). Upgradient wetlands and thermokarst lakes intercept groundwater inflows, increasing connectivity but also simultaneously prolonging flow routing. Precipitation is temporarily stored and recharged into unfrozen, saturated soil, effectively buffering summer precipitation peaks, and then released later during winter through lateral taliks (Ala-aho et al., 2018b), which prolong the recession limbs of downgradient river systems. The development of taliks facilitates vertical connectivity between surface and sub-permafrost groundwater systems, marking a transition toward open-system hydrological dynamics (McKenzie et al., 2021). These processes collectively enhance winter baseflow and advance river-ice breakup timing, contributing to a progressive flattening of seasonal hydrographs (Figure 6c).

Long-term hydrograph evolution revealed fundamental elevational controls on thaw-source partitioning (Figure 6b). The observed increase in Yellow River discharge during 1956–1975 coincided with the rising line of

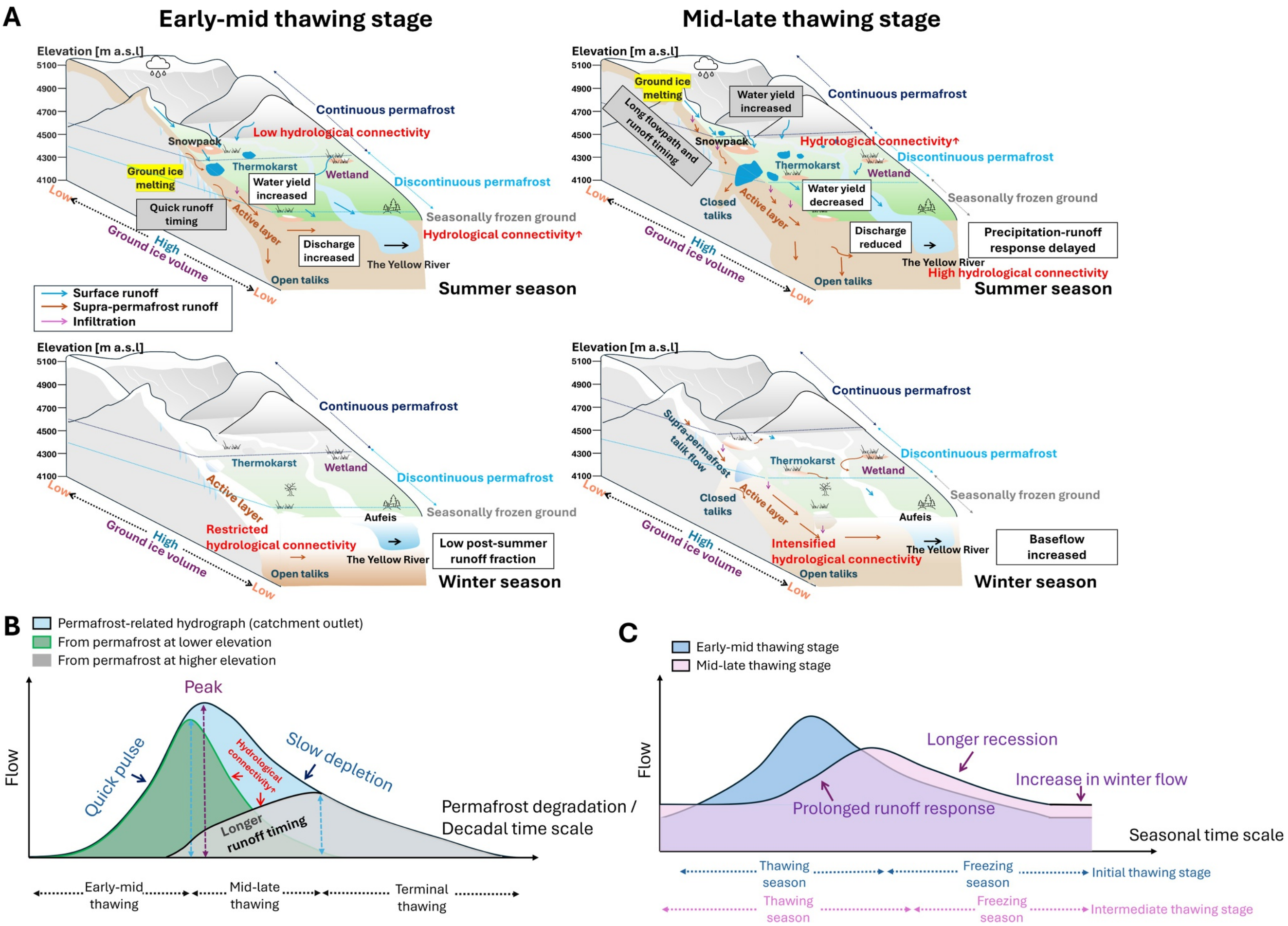

Figure 6. Conceptual model of elevation-dependent hydrological transitions during permafrost degradation. (a) Schematic illustrating progressive alteration in surface and subsurface flows and hydrological connectivity, water yields and streamflow (Yellow River catchment) during summer and winter at early-mid and mid-late permafrost thaw stages. Climate-induced permafrost degradation in SAYR is expected to induce upward shifts in zones of discontinuous permafrost and SFG. Ground ice distribution (based on Figure S1C in Supporting Information S1) indicates that mid-elevation terrain contains substantially more ground ice reserves than low-altitude plains and high-altitude mountainous areas. (b) Conceptual hydrograph of permafrost-thaw related runoff at the catchment outlet (Yellow River) over several decades under permafrost degradation. Note that the time scale is uncertain. To illustrate the altitude effect, permafrost-thaw related runoff is differentiated by low- and high-elevation sources. (c) Conceptual seasonal hydrographs for the watershed at the early-mid and mid-late stages of permafrost degradation, illustrating the delayed runoff effect.

the thaw-driven hydrograph, despite stable precipitation levels, indicating a dominant contribution from low-elevation permafrost thaw. The subsequent decline (1976–1997) reflected diminishing inputs from mid- to low-elevation permafrost near river corridors, with minimal contributions from more distal, higher-elevation sources. The mid- to late-stage thaw transition was marked by the attenuation of the recession hydrograph line, driven by the reorganisation of the flow path. A weakened precipitation-runoff response emerged, with summer-autumn precipitation increasingly contributing to winter baseflow. Intra-annual hydrographs also become progressively flattened (Figure 6c). Collectively, this elevational sequencing imprinted a characteristic "stair-step" degradation signature onto the hydrograph, wherein legacy responses from lower elevations modulate current high-elevation runoff, temporally buffering catchment-scale hydrological dynamics.

4. Summary

4.1. Uncertainties in Water Yield Simulations

To transparently evaluate the robustness of our basin-scale projections, it is essential to distinguish between three primary sources of uncertainty inherent in our framework: (a) machine-learning model uncertainty, (b) input-data uncertainty, and (c) climate-forcing uncertainty. Despite these inherent limitations, the space-for-time

10.1029/2025EF007809

analogue is an effective approach for tracking the hydrological impacts of permafrost degradation at the catchment scale. By integrating snapshots of stable water isotopes (δ^{18}O, δ^{2}H) from thermokarst lakes, characterized by low interannual variability and spanning heterogeneous watershed features, our isotope-enabled machine learning models demonstrate strong upscaling capacity. These models enabled the reconstruction of past conditions and the projection of future large-scale hydrological shifts. Firstly, using a stacked ensemble algorithm reduced biases inherent to individual algorithms, significantly reducing model structural uncertainty (Y. Li et al., 2025).

Secondly, while this historically grounded perspective offers a novel framework for understanding and predicting hydrological trends, we acknowledge the limitations absolute quantification and prediction arising from input-data uncertainty. These constraints primarily arise from the availability and quality of input data, such as field observations, remote sensing reanalysis, as well as the sensitivity and uncertainty inherent in isotope balance models used to derive hydrological indicators (MacDonald et al., 2016). As a result, our quantitative estimations of basin-scale water yield should be interpreted as preliminary baselines rather than definitive absolute values. Although sensitivity analysis indicates that uncertainties in historical and contemporary simulations were well-controlled, the refined inflow characterization may enhance accuracy (Gibson et al., 2019).

Observational data sets in remote cryosphere regions, such as the Arctic and the Qinghai-Tibet Plateau (QTP), are often severely limited due to logistical challenges and high operational costs. Consequently, data collected over short time windows are frequently, by necessity, assumed to represent regional norms (Kang et al., 2017). While such low-resolution sampling may suffice for large basins, capturing the complex water source dynamics of short-residence lakes requires constraining seasonal variability (Haig et al., 2021). Addressing this, our multi-seasonal sampling strategy explicitly characterised these short-term fluctuations. Repeated sampling identified a distinct ‘interannual isotopic reset' mechanism: rapid spring-summer meltwater inputs transition into winter groundwater recharge, producing a well-mixed signal by the following spring. This repeatable cycle shows that our seasonal snapshots represent consistent hydrological states rather than transient noise.

Further concerns regarding the temporal representativeness of our input data are mitigated by converging physical and empirical evidence. Meteorological benchmarking confirms that the sampling period is consistent with baseline conditions. More importantly, the thermal gradient across the >700 m elevation range far exceeds interannual variability, meaning the “space-for-time” substitution is governed by stable geomorphological controls rather than short-term weather fluctuations. Multi-decadal satellite observations corroborate this, aligning with our isotope-derived water balance calculations and confirming that the data set captures long-term structural trends. The “regional lake suite” approach further integrates coherent environmental drivers, such as aridity and thaw-source contributions, that dominate over site-specific noise (Akers et al., 2024). Strong topographic forcing, therefore, suppresses local heterogeneity and provides the robust baseline required to distinguish direct permafrost meltwater inputs from thaw-induced alterations in hydrological connectivity, supporting accurate hydrological modelling (Harning et al., 2024).

Finally, in future projections, the dominant source of uncertainty shifts from internal model structure and baseline data to external climate-forcing prediction. This reflects the irreducible variability among global climate models, particularly in representing precipitation patterns and cryospheric feedback mechanisms under divergent SSPs. Consequently, the projections should be interpreted as a bounded range of plausible hydrological responses to warming rather than deterministic forecasts, emphasising the importance of adaptive planning under high-emission future scenarios.

Even so, this integrated approach provides a robust and verifiable framework for trend assessment and offers a first-order approximation of how hydrological responses propagate across the basin as permafrost degradation intensifies. Thermokarst lakes are valuable indicators of permafrost thaw across both spatial and temporal scales. Paleolimnological analyses of these lake archives offer insights into the long-term evolution of permafrost and its associated hydrological consequences (Bouchard et al., 2016). Our study advanced this field by integrating these site-specific snapshots with machine learning methods to achieve a true basin-scale quantification. This framework also enables assessments of regional WY responses to precipitation variability across historical and projected future periods.

4.2. Hydrological Perspectives

Following permafrost thaw, mountain permafrost regions are projected to undergo accelerated warming (Noetzli et al., 2024). Our isotope-mass balance framework offers a more refined interpretation: the basin is currently experiencing a transient hydrological pulse. Recent modeling studies revealed that climate warming will continue to intensify permafrost degradation across the QTP under various SSP scenarios, triggering complex hydrological reorganisation (Hu et al., 2022). Our projections of gridded terrestrial WY changes are consistent with established hydrological forecasts, including a 9.7% reduction in annual discharge from the Yellow River relative to historic minima (Wang et al., 2023). Recent simulations also demonstrated that runoff components are highly elevation-dependent, resulting in distinct spatial sensitivities to climate forcing (He et al., 2025). Under high-emission scenarios, intensified warming and precipitation may partially offset straightforward declines in WY, as reflected in net annual runoff increases (Wang, Li, Biswas, et al., 2025, Wang, Li, & Liu, 2025; You et al., 2020). Additionally, recent findings highlighted that raising precipitation contributes to deepening the active layer and further warming permafrost (Fu et al., 2025).

Our findings reveal a pronounced elevational dichotomy in hydrological regimes, spanning from thawing permafrost zones to seasonally frozen landscapes. Unlike the gradual trajectory of climate warming, permafrost degradation can occur in non-linear pulses over sub-decadal timescales (Ding et al., 2025). Compared with previous studies that often treated hydrological connectivity as a static binary state (Yang et al., 2019), our results characterized an elevation-dependent connectivity regime specific to high-relief systems, which exhibits marked spatial heterogeneity (Zhang, Väliranta, et al., 2022, Zhang, Nan, & Mu, 2022), as well as disproportionately affecting local WY capacity (Liljedahl et al., 2021). We acknowledge that permafrost distribution is physically governed by a multivariate energy balance, and relying on elevation bands inherently smooths over local thermal heterogeneity driven by aspect or vegetation. While this assumption introduces potential biases at the sub-catchment scale, elevation remains the dominant first-order control on regional permafrost stability in this high-relief terrain (J. Li et al., 2016). The robustness of these elevation thresholds across the study area is validated by the convergence of independent evidence: the "rise-and-fall" pattern identified by water isotope tracer mirrors satellite observations of lake physical dynamics. Disentangling the universal hydrological signatures of permafrost systems requires multi-site investigations, which offer critical insights into evolving regional-scale hydrological dynamics and their sensitivity to changing climate.

This distinct elevation-dependent hydrological connectivity has profound implications for basin-scale hydrological transition and discharge timing. Beyond shifts in annual runoff contributions, landscape transformation and changing hydrological connectivity over recent decades have delayed the confluence timing of thaw-sourced water, reshaping the hydrograph and altering both the timing and magnitude of exported water fluxes (Cochand et al., 2019; Rawlins & Karmalkar, 2023). Quantifying the long-term sensitivity of hydrographs remains challenging due to the complex interplay of climatic drivers and landscape evolution.

Higher-elevation permafrost zones characterized by greater ground ice contents per unit area (Liu et al., 2025; Wang et al., 2018), are projected to gain increasing hydrological importance. Higher-elevation lake-watershed systems (>4,600 m; continuous permafrost) exhibit limited variability in hydrological behavior and are characterized by precipitation-dominated inflows. This reflects continuous permafrost conditions where limited talik development restricts vertical infiltration, consistent with observation from northern Canada (Boreux et al., 2021). This stability is globally significant; mountain regions typically exhibit lower interannual runoff variability compared to lowlands, acting as critical buffers that lowlands increasingly rely upon, particularly during years of low lowland water availability (Hanus et al., 2025). Increasing reliance on permafrost thaw sources in the future will presumably buffer the sensitivity to short-term changes in climatic forcing, although the risk of future drought also increases due to thermal processes related to permafrost degradation (Chen et al., 2023). In contrast, low-elevation river valley plains, dominated by SFG and sporadic permafrost, feature enhanced vertical connectivity. The development of through-going taliks enables drainage via intermediate and deep subsurface pathways, bypassing conventional shallow groundwater recharge mechanisms (Koch et al., 2024). This shift to deeper subsurface routing increases water residence time and imposes a substantial delaying effect on catchment-scale outflows. As permafrost degrades, the basin transitions from a regime dominated by rapid, high-elevation surface inputs to one increasingly modulated by slow, low-elevation subsurface pathways. Quantifying the long-term sensitivity of hydrographs to this evolving connectivity remains challenging but highlights the critical need for integrated, process-based modeling approaches in future water resources assessments. For the middle and lower reaches of the Yellow River, where predictable seasonal pulses underpin agriculture and sediment management, this regime shift poses significant risks (Wang et al., 2023). A transition toward higher winter flows and reduced summer availability would exacerbate the imbalance between water supply and demand, therefore, a fundamental re-evaluation of reservoir management and agricultural planning in the Asian Water Tower is urgent (Hu et al., 2025; L. Li et al., 2025).

4.3. Broader Implications for Biochemical Dynamics

A recent study identified contrasting patterns of greenhouse gas source and sink between high-altitude and high-latitude permafrost regions, driven largely by differences in soil moisture regimes (Bao et al., 2025). A significant knowledge gap persists concerning the response of carbon, nutrients and other solutes stored in long-undisturbed frozen soil and closed aquatic ecosystems to permafrost degradation (Ala-aho et al., 2021; Jiang et al., 2025; Vonk et al., 2015). While high-altitude lakes on the QTP were emerging carbon sinks (Wang, Li, Biswas, et al., 2025, Wang, Li, & Liu, 2025), previous studies highlighted lateral exports of both old and young carbon by permafrost draining rivers (Wild et al., 2019), along with enhanced riverine CO_2 emissions and methane fluxes from the rapidly expanding thermokarst lakes (Mu et al., 2025). As permafrost-river hydrogeological connectivity intensifies, this process is expected to propagate toward higher elevations, fundamentally restructuring carbon delivery pathways. Despite limited soil CO_2 loss being expected from high-elevation permafrost thaw (Deng et al., 2025), lateral transport mechanisms of hydrological movement remain poorly understood (Lemieux et al., 2025). Higher DOC exports are anticipated as ongoing permafrost degradation accelerates the flushing of DOC from deeper, previously frozen soil horizons in higher-elevation zones into streams (Hirst et al., 2022). Simultaneously, thaw-induced deepening of flow paths significantly increases water erosion and subsurface water supply containing nutrients and biologically limiting elements, which promotes microbial growth and metabolism (Hong et al., 2025; Yu et al., 2022). This enhances the consumption of DOM in both soils and rivers, releasing substantial amounts of old carbon unexpectedly during the longer ice-off season (Lynch et al., 2019).

Moreover, downstream valley lowlands and lake wetlands exhibit extended hydrological responsiveness, primarily governed by groundwater recharge. This hydrological regime promotes the gradual accumulation of waterborne metals, which readily bind to DOM. Through burial processes, such interactions may shift aquatic systems from net carbon sources to carbon sinks (Wright et al., 2022). These pronounced hydrological shifts suggest that post-thaw watersheds are likely to transition toward groundwater-dominated regimes. A biogeochemical shift toward aquifer-controlled flow dynamics, characterized by reduced runoff ratios, is anticipated following the complete degradation of permafrost, although future increases in precipitation may partially obscure this effect (Jorgenson et al., 2025). Our refined conceptual model holds strong potential for forecasting long-term hydro-biogeochemical trajectories under progressive permafrost degradation.

Conflict of Interest

The authors declare no conflicts of interest relevant to this study.

Availability Statement

All original isotope data, derived hydrological indicators, machine learning model outputs generated during this study as well as codes are openly available in the Figshare repository (https://doi.org/10.6084/m9.figshare.30435604) (Wan et al., 2026). Gridded reanalysis climate parameters for IMB modelling, including air temperature, relative humidity, precipitation, and potential pan evaporation rates, were derived from ERA5-Land post-processed daily statistics (Copernicus Climate Change Service, Climate Data Store, 2024). Lake surface areas were derived from the long-term data sets on lake number and size across the Tibetan Plateau (1995–2015), specifically using spatial distribution maps of lakes to extract attributes for the SAYR region (Observational & Geospatial, 2018). Vegetation coverage was derived from Wang. (2019). Soil water content was derived from Wang and Yang (2021). DEM data was available from Luo et al. (2011). Mean annual ground temperature and Active layer thickness data were extracted from Ran et al. (2021). Permafrost coverage data was extracted from Zhao. (2019). Ground ice content data was extracted from Zou et al. (2023). Annual changes of active layer thickness data were extracted from Yan et al. (2023). Permafrost instability index was derived from Ran (2019). Future climate data was extracted from Luo et al. (2024). Mean annual ground temperature predictions of 2046–2065 was extracted from Zhao et al. (2025), mean annual ground temperature predictions of 2061–2080 was extracted from Ni and Wu (2021). Future active layer thickness data was extracted from Peng (2022). Future permafrost coverage data was extracted from Zhang, Väliranta, et al. (2022) and Zhang, Nan, and Mu. (2022).

Acknowledgments
This work was supported by the National Natural Science Foundation of China (42207363 and 42571172), Postdoctoral Science Foundation of China (2021M703300), and Jiangsu Postdoctoral Research Funding Program (2021K314C). Contributions by JJG were supported by a Strategic Investment Grant (43110245) from InnoTech Alberta. We sincerely thank Prof. Huijun Jin and Prof. Dongliang Luo (Northwest Institute of Eco-Environment and Resources, Chinese Academy of Sciences), along with their research team and staff, for their assistance in organising and conducting the fieldwork and sampling campaigns. Special thanks go to Paul Eby (InnoTech Alberta) for his analytical support with the stable isotope measurements. We also express our deep gratitude to Prof. Zhongbo Yu (Hohai University) for his insightful guidance, and to Dr. Yi Yi (Government of Alberta) for helpful discussions during the early stages of this research. Finally, we thank the Editor and the two anonymous reviewers for their highly constructive comments and valuable suggestions, which significantly improved the quality of this manuscript. Open access publishing facilitated by The University of Western Australia, as part of the Wiley - The University of Western Australia agreement via the Council of Australasian University Librarians.

References

Akers, P. D., Kopec, B. G., Klein, E. S., Bailey, H., & Welker, J. M. (2024). The pivotal role of evaporation in lake water isotopic variability across space and time in a high Arctic periglacial landscape. *Water Resources Research*, *60*(10), e2023WR036121. https://doi.org/10.1029/2023wr036121

Ala-Aho, P., Autio, A., Bhattacharjee, J., Isokangas, E., Kujala, K., Marttila, H., et al. (2021). What conditions favor the influence of seasonally frozen ground on hydrological partitioning? A systematic review. *Environmental Research Letters*, *16*(4), 043008. https://doi.org/10.1088/1748-9326/abe82c

Ala-Aho, P., Soulsby, C., Pokrovsky, O. S., Kirpotin, S. N., Karlsson, J., Serikova, S., et al. (2018a). Permafrost and lakes control river isotope composition across a boreal Arctic transect in the Western Siberian lowlands. *Environmental Research Letters*, *13*(3), 034028. https://doi.org/10.1088/1748-9326/aaa4fe

Ala-Aho, P., Soulsby, C., Pokrovsky, O. S., Kirpotin, S. N., Karlsson, J., Serikova, S., et al. (2018b). Using stable isotopes to assess surface water source dynamics and hydrological connectivity in a high-latitude wetland and permafrost influenced landscape. *Journal of Hydrology*, *556*, 279–293. https://doi.org/10.1016/j.jhydrol.2017.11.024

Bao, T., Xu, X., Jia, G., Zhu, X., Riley, W. J., & Yang, Y. (2025). Climate-carbon feedback tradeoff between Arctic and alpine permafrost under warming. *Science Advances*, *11*(38), eadt8366. https://doi.org/10.1126/sciadv.adt8366

Biskaborn, B. K., Smith, S. L., Noetzli, J., Matthes, H., Vieira, G., Streletskiy, D. A., et al. (2019). Permafrost is warming at a global scale. *Nature Communications*, *10*(1), 264. https://doi.org/10.1038/s41467-018-08240-4

Boreux, M. P., Lamoureux, S. F., & Cumming, B. F. (2021). Use of water isotopes and chemistry to infer the type and degree of exchange between groundwater and lakes in an esker complex of northeastern Ontario, Canada. *Hydrology and Earth System Sciences*, *25*(12), 6309–6332. https://doi.org/10.5194/hess-25-6309-2021

Bouchard, F., MacDonald, L. A., Turner, K. W., Thienpont, J. R., Medeiros, A. S., Biskaborn, B. K., et al. (2016). Paleolimnology of thermokarst lakes: A window into permafrost landscape evolution. *Arctic Science*, *3*(2), 91–117. https://doi.org/10.1139/as-2016-0022

Brand, W. A., Avak, H., Seedorf, R., Hofmann, D., & Conradi, T. (1996). New methods for fully automated isotope ratio determination from hydrogen at the natural abundance level. *Isotopes in Environmental and Health Studies*, *32*(2–3), 263–273. https://doi.org/10.1080/10256019608036319

Bring, A., Fedorova, I., Dibike, Y., Hinzman, L., Mård, J., Mernild, S. H., et al. (2016). Arctic terrestrial hydrology: A synthesis of processes, regional effects, and research challenges. *Journal of Geophysical Research: Biogeosciences*, *121*(3), 621–649. https://doi.org/10.1002/2015jg003131

Bring, A., Shiklomanov, A., & Lammers, R. B. (2017). Pan-Arctic river discharge: Prioritizing monitoring of future climate change hot spots. *Earth's Future*, *5*(1), 72–92. https://doi.org/10.1002/2016ef000434

Chen, Y., Cheng, X., Liu, A., Chen, Q., & Wang, C. (2023). Tracking lake drainage events and drained lake basin vegetation dynamics across the Arctic. *Nature Communications*, *14*(1), 7359. https://doi.org/10.1038/s41467-023-43207-0

Cochand, M., Christe, P., Ornstein, P., & Hunkeler, D. (2019). Groundwater storage in high alpine catchments and its contribution to streamflow. *Water Resources Research*, *55*(4), 2613–2630. https://doi.org/10.1029/2018wr022989

Connon, R. F., Quinton, W. L., Craig, J. R., & Hayashi, M. (2014). Changing hydrologic connectivity due to permafrost thaw in the lower Liard River valley, NWT, Canada. *Hydrological Processes*, *28*(14), 4163–4178. https://doi.org/10.1002/hyp.10206

Copernicus Climate Change Service, Climate Data Store. (2024). ERA5-land post-processed daily-statistics from 1950 to present. *Copernicus Climate Change Service (C3S) Climate Data Store (CDS)*. [Dataset]. https://doi.org/10.24381/cds.e9c9c792

Deng, Z., Fan, J., Wei, D., Qi, Y., Tao, J., Wang, Z., et al. (2025). The negative elevation-dependent pattern of non-growing season CO2 loss from alpine frozen ground. *Geophysical Research Letters*, *52*(8), e2024GL113490. https://doi.org/10.1029/2024gl113490

Ding, K., Jiang, P., Ni, J., Shen, T., Yang, B., Zhang, R., & Yu, Z. (2025). Machine learning uncovers a multi-year climate memory in permafrost degradation on the Qinghai–Tibet Plateau: The critical roles of precipitation and lagged temperature. *Journal of Hydrology*, *663*, 134272. https://doi.org/10.1016/j.jhydrol.2025.134272

Fryda, T., LeDell, E., Gill, N., Aiello, S., Fu, A., Candel, A., et al. (2023). h2o: R interface for the 'H2O' scalable machine learning platform. *R package version 3.40.0.4*. https://CRAN.R-project.org/package=h2o

Fu, Z., Qingbai, W., Anping, C., Luyang, W., Guanli, J., Siru, G., et al. (2025). Non-temperature environmental drivers modulate warming-induced 21st-century permafrost degradation on the Tibetan Plateau. *Nature Communications*, *16*(1), 7556. https://doi.org/10.1038/s41467-025-63032-x

Gao, H., Wang, J., Yang, Y., Pan, X., Ding, Y., & Duan, Z. (2021). Permafrost hydrology of the Qinghai-Tibet Plateau: A review of processes and modeling. *Frontiers in Earth Science*, *8*, 576838. https://doi.org/10.3389/feart.2020.576838

Gao, T., Zhang, T., Cao, L., Kang, S., & Sillanpää, M. (2016). Reduced winter runoff in a mountainous permafrost region in the northern Tibetan Plateau. *Cold Regions Science and Technology*, *126*, 36–43. https://doi.org/10.1016/j.coldregions.2016.03.007

Gibson, J. J., Birks, S. J., & Yi, Y. (2016). Stable isotope mass balance of lakes: A contemporary perspective. *Quaternary Science Reviews*, *131*, 316–328. https://doi.org/10.1016/j.quascirev.2015.04.013

Gibson, J. J., Birks, S. J., Yi, Y., Shaw, P., & Moncur, M. C. (2018). Isotopic and geochemical surveys of lakes in coastal BC: Insights into regional water balance and water quality controls. *Journal of Hydrology: Regional Studies*, *17*, 47–63. https://doi.org/10.1016/j.ejrh.2018.04.006

Gibson, J. J., & Prowse, T. D. (1999). Isotopic characteristics of ice cover in a large northern river basin. *Hydrological Processes*, *13*(16), 2537–2548. https://doi.org/10.1002/(sici)1099-1085(199911)13:16<2537::aid-hyp940>3.3.co;2-1

Gibson, J. J., & Prowse, T. D. (2002). Stable isotopes in river ice: Identifying primary over-winter streamflow signals and their hydrological significance. *Hydrological Processes*, *16*(4), 873–890. https://doi.org/10.1002/hyp.366

Gibson, J. J., Yi, Y., & Birks, S. J. (2019). Isotopic tracing of hydrologic drivers including permafrost thaw status for lakes across Northeastern Alberta, Canada: A 16-year, 50-lake assessment. *Journal of Hydrology: Regional Studies*, *26*, 100643. https://doi.org/10.1016/j.ejrh.2019.100643

Google. (n.d.). Google Earth pro satellite imagery of the source area of the yellow river (SAYR). Retrieved from https://earth.google.com

Guo, L., Wang, G., Song, C., Sun, S., Li, J., Li, K., et al. (2025). Hydrological changes caused by integrated warming, wetting, and greening in permafrost regions of the Qinghai-Tibetan Plateau. *Water Resources Research*, *61*(4), e2024WR038465. https://doi.org/10.1029/2024wr038465

Haig, H. A., Hayes, N. M., Simpson, G. L., Yi, Y., Wissel, B., Hodder, K. R., & Leavitt, P. R. (2021). Effects of seasonal and interannual variability in water isotopes (δ^2H, δ^{18}O) on estimates of water balance in a chain of seven prairie lakes. *Journal of Hydrology X*, *10*, 100069. https://doi.org/10.1016/j.hydroa.2020.100069

Han, L., & Menzel, L. (2024). Hydrological response to long-lasting dry spell at the southern edge of Siberian permafrost. *Science of the Total Environment*, *922*, 171330. https://doi.org/10.1016/j.scitotenv.2024.171330

Hanus, S., Burek, P., Smilovic, M., Seibert, J., Wada, Y., & Viviroli, D. (2025). Dependence of lowland water use on mountain runoff globally: Interannual variability and future changes at seasonal scale. *Earth's Future*, *13*(10), e2025EF006407. https://doi.org/10.1029/2025ef006407

Harning, D., Raberg, J., McFarlin, J., Axford, Y., Florian, C., Ólafsdóttir, K., et al. (2024). Spatiotemporal variation of modern lake, stream, and soil water isotopes in Iceland. *Hydrology and Earth System Sciences Discussions*, *2024*(18), 1–35. https://doi.org/10.5194/hess-28-4275-2024

He, B., Chang, J., Guo, A., Wang, L., Li, Z., Zhai, D., & Gao, F. (2025). Spatial and temporal runoff variability in response to climate change in alpine mountains. *Journal of Hydrology*, *654*, 132779. https://doi.org/10.1016/j.jhydrol.2025.132779

Hirst, C., Mauclet, E., Monhonval, A., Tihon, E., Ledman, J., Schuur, E. A., & Opfergelt, S. (2022). Seasonal changes in hydrology and permafrost degradation control mineral element-bound DOC transport from permafrost soils to streams. *Global Biogeochemical Cycles*, *36*(2), e2021GB007105. https://doi.org/10.1029/2021gb007105

Hong, J., Pang, B., Zhao, L., Shu, S., Feng, P., Liu, F., et al. (2025). Soil phosphorus crisis in the Tibetan alpine permafrost region. *Nature Communications*, *16*(1), 6204. https://doi.org/10.1038/s41467-025-61501-x

Horita, J., Rozanski, K., & Cohen, S. (2008). Isotope effects in the evaporation of water: A status report of the Craig–Gordon model. *Isotopes in Environmental and Health Studies*, *44*(1), 23–49. https://doi.org/10.1080/10256010801887174

Horita, J., & Wesolowski, D. J. (1994). Liquid-vapor fractionation of oxygen and hydrogen isotopes of water from the freezing to the critical temperature. *Geochimica et Cosmochimica Acta*, *58*(16), 3425–3437. https://doi.org/10.1016/0016-7037(94)90096-5

Hu, G., Zhao, L., Wu, T., Wu, X., Park, H., Li, R., et al. (2022). Continued warming of the permafrost regions over the Northern hemisphere under future climate change. *Earth's Future*, *10*(9), e2022EF002835. https://doi.org/10.1029/2022ef002835

Hu, J., Zhou, X., Yi, Y., Li, C., Wang, X., Liu, Q., & Mao, J. (2025). Hydrological changes in the upper yellow river under the impact of upstream cascade reservoirs over the past 70 years. *Journal of Hydrology: Regional Studies*, *57*, 102105. https://doi.org/10.1016/j.ejrh.2024.102105

Jiang, C., Li, D., Gao, Y., Liu, W., & Zhang, L. (2017). Impact of climate variability and anthropogenic activity on streamflow in the three Rivers headwater Region, Tibetan Plateau, China. *Theoretical and Applied Climatology*, *129*(1), 667–681. https://doi.org/10.1007/s00704-016-1833-7

Jiang, G., Men, X., Fu, Z., Zeng, L., Hu, W., Gao, S., & Wu, Q. (2025). Thaw slumps alter ecosystem carbon budget in alpine grassland on the Tibetan Plateau. *Nature Communications*.

Jin, H., He, R., Cheng, G., Wu, Q., Wang, S., Lü, L., & Chang, X. (2009). Changes in frozen ground in the source area of the yellow river on the Qinghai–TibetPlateau, China, and their eco-environmental impacts. *Environmental Research Letters*, *4*(4), 045206. https://doi.org/10.1088/1748-9326/4/4/045206

Jin, H., Huang, Y., Bense, V. F., Ma, Q., Marchenko, S. S., Shepelev, V. V., et al. (2022). Permafrost degradation and its hydrogeological impacts. *Water*, *14*(3), 372. https://doi.org/10.3390/w14030372

Jin, H. J., Wu, Q. B., & Romanovsky, V. E. (2021). Degrading permafrost and its impacts. *Advances in Climate Change Research*, *12*(1), 1–5. https://doi.org/10.1016/j.accre.2021.01.007

Jorgenson, K. L., Douglas, T. A., Jorgenson, M. T., Pastick, N. J., & Harms, T. K. (2025). Permafrost and rain influence summer hydrologic flowpaths in boreal catchments. *Water Resources Research*, *61*(6), e2024WR039024. https://doi.org/10.1029/2024wr039024

Kang, S., Yi, Y., Xu, Y., Xu, B., & Zhang, Y. (2017). Water isotope framework for Lake water balance monitoring and modelling in the Nam Co Basin, Tibetan Plateau. *Journal of Hydrology: Regional Studies*, *12*, 289–302. https://doi.org/10.1016/j.ejrh.2017.05.007

Koch, J. C., Connolly, C. T., Baughman, C., Repasch, M., Best, H., & Hunt, A. (2024). The dominance and growth of shallow groundwater resources in continuous permafrost environments. *Proceedings of the National Academy of Sciences*, *121*(23), e2317873121. https://doi.org/10.1073/pnas.2317873121

Krogh, S. A., & Pomeroy, J. W. (2018). Recent changes to the hydrological cycle of an Arctic basin at the tundra–taiga transition. *Hydrology and Earth System Sciences*, *22*(7), 3993–4014. https://doi.org/10.5194/hess-22-3993-2018

Lafrenière, M. J., & Lamoureux, S. F. (2019). Effects of changing permafrost conditions on hydrological processes and fluvial fluxes. *Earth-Science Reviews*, *191*, 212–223. https://doi.org/10.1016/j.earscirev.2019.02.018

Lemieux, J. M., Frampton, A., & Fortier, P. (2025). Recent advances (2018–2023) and research opportunities in the study of groundwater in cold regions. *Permafrost and Periglacial Processes*, *36*(1), 93–109. https://doi.org/10.1002/ppp.2255

Li, J. (2020). Distribution data of permafrost in the source area of the Yellow River (2013–2015). National Tibetan Plateau/Third Pole Environment Data Center [Dataset]. https://doi.org/10.11888/Geocry.tpdc.270932

Li, J., Sheng, Y., Wu, J., Feng, Z., Ning, Z., Hu, X., & Zhang, X. (2016). Landform-related permafrost characteristics in the source area of the Yellow River, eastern Qinghai-Tibet Plateau. *Geomorphology*, *269*, 104–111. https://doi.org/10.1016/j.geomorph.2016.06.024

Li, L., He, C., Huang, Q., Liu, Z., Li, J., Zhao, K., et al. (2025). Growing imbalance between supply and demand for flood regulation service in the Asian water tower and its downstream region. *Earth's Future*, *13*(9), e2025EF006338. https://doi.org/10.1029/2025ef006338

Li, Y., Han, D., Rogers, C. A., Finkelstein, S. A., Hararuk, O., Waddington, J. M., et al. (2025). Peat depth and carbon storage of the Hudson Bay Lowlands, Canada. *Geophysical Research Letters*, *52*(2), e2024GL110679. https://doi.org/10.1029/2024GL110679

Liljedahl, L. C., Meierbachtol, T., Harper, J., van As, D., Näslund, J. O., Selroos, J. O., et al. (2021). Rapid and sensitive response of Greenland's groundwater system to ice sheet change. *Nature Geoscience*, *14*(10), 751–755. https://doi.org/10.1038/s41561-021-00813-1

Lindsay, J. B. (2016). Whitebox GAT: A case study in geomorphometric analysis. *Computers & Geosciences*, *95*, 75–84. https://doi.org/10.1016/j.cageo.2016.07.003

Liu, S., Zhou, H., Zhao, L., Wang, L., Zou, D., Hu, G., et al. (2025). The ground ice melting has accelerated the lake expansion in the hinterland of the permafrost region on the Qinghai-Tibet Plateau. *Journal of Hydrology: Regional Studies*, *58*, 102268. https://doi.org/10.1016/j.ejrh.2025.102268

Luo, D., Jin, H., Wu, Q., Bense, V. F., He, R., Ma, Q., et al. (2018). Thermal regime of warm-dry permafrost in relation to ground surface temperature in the source areas of the Yangtze and Yellow rivers on the Qinghai-Tibet Plateau, SW China. *Science of the Total Environment*, *618*, 1033–1045. https://doi.org/10.1016/j.scitotenv.2017.09.083

Luo, D. L., Jin, H. J., Jin, R., Lin, L., He, R. X., & Chang, X. L. (2011). The extraction of watershed characteristics of the source area of yellow river based on SRTM DEM with ArcGIS, IEEE (in Chinese). *IEEE Xplore: International Conference on Remote Sensing, Environment and Transportation Engineering (RSETE2011)*. https://doi.org/10.1109/RSETE.2011.5964645

Luo, Y., Yuan, H., & Ning, L. (2024). HiCPC: High-resolution CMIP6 downscaled daily climate projections over China 1979-2100. *National Tibetan Plateau / Third Pole Environment Data Center*. [Dataset]. https://doi.org/10.11888/Atmos.tpdc.301122

Lütjen, M., Overduin, P. P., Juhls, B., Boike, J., Morgenstern, A., & Meyer, H. (2024). Drivers of winter ice formation on arctic water bodies in the Lena Delta, Siberia. *Arctic Antarctic and Alpine Research*, *56*(1), 2350546. https://doi.org/10.1080/15230430.2024.2350546
Lynch, L. M., Machmuller, M. B., Boot, C. M., Covino, T. P., Rithner, C. D., Cotrufo, M. F., et al. (2019). Dissolved organic matter chemistry and transport along an Arctic tundra hillslope. *Global Biogeochemical Cycles*, *33*(1), 47–62. https://doi.org/10.1029/2018gb006030
Ma, Q., Hui-Jun, J., Victor, F. B., Dong-Liang, L. U. O., Sergey, S. M., Stuart, A. H., & Yong-Chao, L. (2019). Impacts of degrading permafrost on streamflow in the source area of Yellow River on the Qinghai-Tibet Plateau, China. *Advances in Climate Change Research*, *10*(4), 225–239. https://doi.org/10.1016/j.accre.2020.02.001
Ma, Q., Jin, H. J., Wu, Q. B., Yurova, A., Liang, S. H., Şerban, R. D., & Lan, Y. C. (2023). Changes in hydrological processes in the headwater area of Yellow river, China during 1956–2019 under the influences of climate change, permafrost thaw and dam. *Advances in Climate Change Research*, *14*(2), 237–247. https://doi.org/10.1016/j.accre.2023.03.006
MacDonald, L. A., Wolfe, B. B., Turner, K. W., Anderson, L., Arp, C. D., Birks, S. J., et al. (2016). A synthesis of thermokarst lake water balance in high-latitude regions of North America from isotope tracers. *Arctic Science*, *3*(2), 118–149. https://doi.org/10.1139/as-2016-0019
McKenzie, J. M., Kurylyk, B. L., Walvoord, M. A., Bense, V. F., Fortier, D., Spence, C., & Grenier, C. (2021). Invited perspective: What lies beneath a changing Arctic? *The Cryosphere*, *15*(1), 479–484. https://doi.org/10.5194/tc-15-479-2021
Mu, C., Lei, P., Mu, M., Zhang, C., Zhou, Z., Song, J., et al. (2025). Methane emissions from thermokarst lakes must emphasize the ice-melting impact on the Tibetan Plateau. *Nature Communications*, *16*(1), 2404. https://doi.org/10.1038/s41467-025-57745-2
Nadeau, S., Rosa, E., Cloutier, V., Paran, F., Hélie, J. F., & Graillot, D. (2022). Hydrological mass balance of boreal watersheds in the Canadian Shield. *Journal of Hydrology*, *612*, 128236. https://doi.org/10.1016/j.jhydrol.2022.128236
Narancic, B., Wolfe, B. B., Pienitz, R., Meyer, H., & Lamhonwah, D. (2017). Landscape-gradient assessment of thermokarst lake hydrology using water isotope tracers. *Journal of Hydrology*, *545*, 327–338. https://doi.org/10.1016/j.jhydrol.2016.11.028
Nelson, D. D., McManus, J. B., Herndon, S. C., Zahniser, M. S., Tuzson, B., & Emmenegger, L. (2008). New method for isotopic ratio measurements of atmospheric carbon dioxide using a 4.3 μm pulsed quantum cascade laser. *Applied Physics B*, *90*(2), 301–309. https://doi.org/10.1007/s00340-007-2894-1
Ni, J., & Wu, T. (2021). *Simulation data of active layer thickness and ground temperature of permafrost in Qinghai Tibet Plateau (2000-2015, 2061-2080)*. National Tibetan Plateau / Third Pole Environment Data Center.
Nitze, I., Grosse, G., Jones, B. M., Arp, C. D., Ulrich, M., Fedorov, A., & Veremeeva, A. (2017). Landsat-based trend analysis of lake dynamics across northern permafrost regions. *Remote Sensing*, *9*(7), 640. https://doi.org/10.3390/rs9070640
Noetzli, J., Isaksen, K., Barnett, J., Christiansen, H. H., Delaloye, R., Etzelmüller, B., et al. (2024). Enhanced warming of European mountain permafrost in the early 21st century. *Nature Communications*, *15*(1), 10508. https://doi.org/10.1038/s41467-024-54831-9
Observational, a., & Geospatial, D. (2018). Spatial distribution maps of lakes over the Tibetan Plateau (1995-2015). *National Tibetan Plateau / Third Pole Environment Data Center*. [Dataset]. https://doi.org/10.11888/Lake.tpe.249437.file
Paul, D., & Skrzypek, G. (2006). Flushing time and storage effects on the accuracy and precision of carbon and oxygen isotope ratios of sample using the Gasbench II technique. *Rapid Communications in Mass Spectrometry*, *20*(13), 2033–2040. https://doi.org/10.1002/rcm.2559
Peng, X. (2022). Past and projected active layer thickness in permafrost regions across the Northern Hemisphere (1850-2100). *National Tibetan Plateau / Third Pole Environment Data Center*. [Dataset]. https://doi.org/10.11888/Cryos.tpdc.272835
Qin, J., Yang, B., Ding, Y., Cui, J., & Zhang, Y. (2025). Assessment of runoff generation capacity and total runoff contribution for different landscapes in alpine and permafrost watershed. *Catena*, *249*, 108643. https://doi.org/10.1016/j.catena.2024.108643
Qiu, J. (2012). Thawing permafrost reduces river runoff. *Nature*, *6*. https://doi.org/10.1038/nature.2012.9749
Ran, Y. (2019). Permafrost stability type map for Sanjiangyuan in 2010s. *National Tibetan Plateau / Third Pole Environment Data Center*. [Dataset]. https://doi.org/10.11888/Geocry.tpdc.270973
Ran, Y., Li, X., Cheng, G., Che, J., Juha, A., Olli, K., et al. (2021). High-resolution datasets of permafrost thermal state and hydrothermal zonation in the Northern Hemisphere. *National Tibetan Plateau / Third Pole Environment Data Center*. [Dataset]. https://doi.org/10.11888/Geocry.tpdc.271190
Rawlins, M. A., & Karmalkar, A. V. (2023). Regime shifts in Arctic terrestrial hydrology manifested from impacts of climate warming. *The Cryosphere Discussions*, *2023*, 1–38.
R Core Team. (2023). R: A language and environment for statistical computing (Version 4.2.3). *R Foundation for Statistical Computing*. [Computer software] Retrieved from https://www.R-project.org/
Ren, W., Yao, T., Yang, X., & Joswiak, D. R. (2013). Implications of variations in δ18O and δD in precipitation at Madoi in the eastern Tibetan Plateau. *Quaternary International*, *313*, 56–61. https://doi.org/10.1016/j.quaint.2013.05.026
Şerban, R. D., Jin, H., Şerban, M., & Luo, D. (2021). Shrinking thermokarst lakes and ponds on the northeastern Qinghai-Tibet plateau over the past three decades. *Permafrost and Periglacial Processes*, *32*(4), 601–617. https://doi.org/10.1002/ppp.2127
Sheng, Y., Ma, S., Cao, W., & Wu, J. (2020). Spatiotemporal changes of permafrost in the Headwater Area of the Yellow River under a changing climate. *Land Degradation & Development*, *31*(1), 133–152. https://doi.org/10.1002/ldr.3434
Song, C., Wang, G., Sun, X., & Hu, Z. (2021). River runoff components change variably and respond differently to climate change in the Eurasian Arctic and Qinghai-Tibet Plateau permafrost regions. *Journal of Hydrology*, *601*, 126653. https://doi.org/10.1016/j.jhydrol.2021.126653
Song, L., Wang, L., Zhou, J., Luo, D., & Li, X. (2022). Divergent runoff impacts of permafrost and seasonally frozen ground at a large river basin of Tibetan Plateau during 1960–2019. *Environmental Research Letters*, *17*(12), 124038. https://doi.org/10.1088/1748-9326/aca4eb
Stolpmann, L., Nitze, I., Bussmann, I., Jones, B. M., Lenz, J., Meyer, H., & Grosse, G. (2024). *Thermokarst lake change and lake hydrochemistry: A snapshot from the Arctic Coastal Plain of Alaska* (Vol. 2024, pp. 1–34). EGUsphere.
Streletskiy, D. A., Tananaev, N. I., Opel, T., Shiklomanov, N. I., Nyland, K. E., Streletskaya, I. D., & Shiklomanov, A. I. (2015). Permafrost hydrology in changing climatic conditions: Seasonal variability of stable isotope composition in rivers in discontinuous permafrost. *Environmental Research Letters*, *10*(9), 095003. https://doi.org/10.1088/1748-9326/10/9/095003
Turner, K. W., Edwards, T. W., & Wolfe, B. B. (2014). Characterising runoff generation processes in a lake-rich thermokarst landscape (Old Crow Flats, Yukon, Canada) using δ18O, δ2H and d-excess measurements. *Permafrost and Periglacial Processes*, *25*(1), 53–59. https://doi.org/10.1002/ppp.1802
Vonk, J. E., Tank, S. E., Bowden, W. B., Laurion, I., Vincent, W. F., Alekseychik, P., et al. (2015). Reviews and syntheses: Effects of permafrost thaw on Arctic aquatic ecosystems. *Biogeosciences*, *12*(23), 7129–7167. https://doi.org/10.5194/bg-12-7129-2015
Vonk, J. E., Tank, S. E., & Walvoord, M. A. (2019). Integrating hydrology and biogeochemistry across frozen landscapes. *Nature Communications*, *10*(1), 5377. https://doi.org/10.1038/s41467-019-13361-5
Wan, C., Gibson, J. J., & Peters, D. L. (2020). Isotopic constraints on water balance of tundra lakes and watersheds affected by permafrost degradation, Mackenzie Delta region, Northwest Territories, Canada. *Science of the Total Environment*, *731*, 139176. https://doi.org/10.1016/j.scitotenv.2020.139176

Wan, C., Gibson, J. J., Shen, S., Yi, Y., Yi, P., & Yu, Z. (2019). Using stable isotopes paired with tritium analysis to assess thermokarst lake water balances in the source area of the Yellow River, northeastern Qinghai-Tibet Plateau, China. *Science of the Total Environment*, *689*, 1276–1292. https://doi.org/10.1016/j.scitotenv.2019.06.427

Wan, C., Gibson, J. J., Yi, P., Pan, X., Chen, C., & Skrzypek, G. (2026). Elevation-dependent permafrost thaw on the Tibetan Plateau delays seasonal discharge and poses a risk of reduction in downstream water availability. *Figshare*. [Dataset]. https://doi.org/10.6084/m9.figshare.30435604

Wang, G. (2019). The map of fractional vegetation cover in the Yellow River source region of Tibet Plateau (2015). *National Tibetan Plateau / Third Pole Environment Data Center*. [Dataset]. https://doi.org/10.11888/Ecolo.tpdc.270476

Wang, L., Li, Y., Biswas, A., Zhao, Y., Niu, B., & Siddique, K. H. (2025). Assessing climate change and human impacts on runoff and hydrological droughts in the Yellow River Basin using a machine learning-enhanced hydrological modeling approach. *Journal of Environmental Management*, *380*, 125091. https://doi.org/10.1016/j.jenvman.2025.125091

Wang, P., Huang, Q., Pozdniakov, S. P., Liu, S., Ma, N., Wang, T., et al. (2021). Potential role of permafrost thaw on increasing Siberian River discharge. *Environmental Research Letters*, *16*(3), 034046. https://doi.org/10.1088/1748-9326/abe326

Wang, S., Sheng, Y., Li, J., Wu, J., Cao, W., & Ma, S. (2018). An estimation of ground ice volumes in permafrost layers in Northeastern Qinghai-Tibet Plateau, China. *Chinese Geographical Science*, *28*(1), 61–73. https://doi.org/10.1007/s11769-018-0932-z

Wang, T., & Yang, D. (2021). Water balance dataset in the Yellow River source region and Qilian Mountains in the past 40 years (runoff, precipitation, evapotranspiration, soil liquid water content). *National Tibetan Plateau / Third Pole Environment Data Center*. [Dataset]. https://doi.org/10.11888/Terre.tpdc.271952

Wang, T., Yang, D., Yang, Y., Zheng, G., Jin, H., Li, X., et al. (2023). Pervasive permafrost thaw exacerbates future risk of water shortage across the Tibetan Plateau. *Earth's Future*, *11*(10), e2022EF003463. https://doi.org/10.1029/2022ef003463

Wang, Z., Li, X., & Liu, X. (2025). High-altitude lakes have become emerging carbon sinks on the Qinghai-Tibet Plateau. *Earth's Future*, *13*(12), e2025EF006481. https://doi.org/10.1029/2025ef006481

Wild, B., Andersson, A., Bröder, L., Vonk, J., Hugelius, G., McClelland, J. W., et al. (2019). Rivers across the Siberian Arctic unearth the patterns of carbon release from thawing permafrost. *Proceedings of the National Academy of Sciences*, *116*(21), 10280–10285. https://doi.org/10.1073/pnas.1811797116

Wright, S. N., Thompson, L. M., Olefeldt, D., Connon, R. F., Carpino, O. A., Beel, C. R., & Quinton, W. L. (2022). Thaw-induced impacts on land and water in discontinuous permafrost: A review of the Taiga Plains and Taiga Shield, northwestern Canada. *Earth-Science Reviews*, *232*, 104104. https://doi.org/10.1016/j.earscirev.2022.104104

Yan, D., Zheng, X., Feng, M., Liang, S., Hu, Z., Kuang, X., & Feng, Y. (2023). Frozen ground change data set in the Tibetan Plateau (1961-2020). National Tibetan Plateau / Third Pole Environment Data Center. [Dataset]. https://doi.org/10.11888/Cryos.tpdc.300955

Yang, Y., Ji, W., Niu, L., Zheng, Z., Huang, W., Zhang, C., et al. (2024). Assessing satellite and reanalysis-based precipitation products in cold and arid mountainous regions. *Journal of Hydrology: Regional Studies*, *51*, 101612. https://doi.org/10.1016/j.ejrh.2023.101612

Yang, Y., Wu, Q., Jin, H., Wang, Q., Huang, Y., Luo, D., et al. (2019). Delineating the hydrological processes and hydraulic connectivities under permafrost degradation on Northeastern Qinghai-Tibet Plateau, China. *Journal of Hydrology*, *569*, 359–372. https://doi.org/10.1016/j.jhydrol.2018.11.068

Yang, Y., Wu, Q., Liu, F., & Jin, H. (2021). Spatial-temporal trends of hydrological transitions in thermokarst lakes on Northeast Qinghai-Tibet Plateau based on stable isotopes. *Journal of Hydrology*, *597*, 126314. https://doi.org/10.1016/j.jhydrol.2021.126314

Yang, Y., Wu, Q., Yun, H., Jin, H., & Zhang, Z. (2016). Evaluation of the hydrological contributions of permafrost to the thermokarst lakes on the Qinghai–Tibet Plateau using stable isotopes. *Global and Planetary Change*, *140*, 1–8. https://doi.org/10.1016/j.gloplacha.2016.03.006

Yi, Y., Brock, B. E., Falcone, M. D., Wolfe, B. B., & Edwards, T. W. (2008). A coupled isotope tracer method to characterize input water to lakes. *Journal of Hydrology*, *350*(1–2), 1–13. https://doi.org/10.1016/j.jhydrol.2007.11.008

You, Q., Chen, D., Wu, F., Pepin, N., Cai, Z., Ahrens, B., et al. (2020). Elevation dependent warming over the Tibetan Plateau: Patterns, mechanisms and perspectives. *Earth-Science Reviews*, *210*, 103349. https://doi.org/10.1016/j.earscirev.2020.103349

Yu, C., Hua, K., Huang, C. S., Jin, H., Sun, Y., & Yu, Z. (2022). Spatiotemporal characteristics of arsenic and lead with seasonal freeze-thaw cycles in the source area of the Yellow River Tibet Plateau, China. *Journal of Hydrology: Regional Studies*, *44*, 101210. https://doi.org/10.1016/j.ejrh.2022.101210

Yue, S., & Wang, C. Y. (2002). Applicability of prewhitening to eliminate the influence of serial correlation on the mann-kendall test. *Water resources research*, *38*(6). https://doi.org/10.1029/2001wr000861

Zhang, F., Li, H., Li, Y., Guo, X., Dai, L., Lin, L., et al. (2019). Strong seasonal connectivity between shallow groundwater and soil frost in a humid alpine meadow, northeastern Qinghai-Tibetan Plateau. *Journal of Hydrology*, *574*, 926–935. https://doi.org/10.1016/j.jhydrol.2019.05.008

Zhang, G., Mu, C., Nan, Z., Wu, X., & Cheng, G. (2023). Elevation dependency of future degradation of permafrost over the Qinghai-Tibet Plateau. *Environmental Research Letters*, *18*(7), 075005. https://doi.org/10.1088/1748-9326/ace0d1

Zhang, G., Nan, Z., & Mu, C. (2022). Future permafrost distribution over the Qinghai-Tibet Plateau under different SSP scenarios (2016-2100). *National Tibetan Plateau / Third Pole Environment Data Center*. [Dataset]. https://doi.org/10.11888/Cryos.tpdc.300030

Zhang, H., Väliranta, M., Swindles, G. T., Aquino-López, M. A., Mullan, D., Tan, N., et al. (2022a). Recent climate change has driven divergent hydrological shifts in high-latitude peatlands. *Nature Communications*, *13*(1), 4959. https://doi.org/10.1038/s41467-022-32711-4

Zhao, L. (2019). A new map of permafrost distribution on the Tibetan Plateau (2017). *National Tibetan Plateau / Third Pole Environment Data Center*. [Dataset]. https://doi.org/10.11888/Geocry.tpdc.270468

Zhao, L., Zou, D., Hu, G., Wu, T., Du, E., Liu, G., et al. (2021). A synthesis dataset of permafrost thermal state for the Qinghai–Tibet (Xizang) Plateau, China. *Earth System Science Data*, *13*(8), 4207–4218. https://doi.org/10.5194/essd-13-4207-2021

Zhao, Y., Yao, Y., Jin, H., Li, X., Cao, B., Ran, Y., et al. (2025). TTOP model simulation of long-term (1981–2100) permafrost dynamics of the Tibetan Plateau. *Geoderma*, *457*, 117287. https://doi.org/10.1016/j.geoderma.2025.117287

Zou, D., Pang, Q., Zhao, L., Wang, L., Hu, G., Du, E., et al. (2023). Permafrost ground-ice content to 10 m depth on the Qinghai-Tibet Plateau. *National Tibetan Plateau / Third Pole Environment Data Center*. [Dataset]. https://doi.org/10.11888/Cryos.tpdc.300748